Progress In Electromagnetics Research, Vol. 164, 27–61, 2019

On the Convergence of Numerical Computations for Both Exact and Approximate Solutions for Electromagnetic Scattering by Nonspherical Dielectric Particles

Ping Yang[1, *], Jiachen Ding[1], Richard Lee Panetta[1], Kuo-Nan Liou[2], George W. Kattawar[3], and Michael Mishchenko[4]

(*Invited Paper*)

Abstract—We summarize the size parameter range of the applicability of four light-scattering computational methods for nonspherical dielectric particles. These methods include two exact methods — the extended boundary condition method (EBCM) and the invariant imbedding T-matrix method (II-TM) and two approximate approaches — the physical-geometric optics method (PGOM) and the improved geometric optics method (IGOM). For spheroids, the single-scattering properties computed by EBCM and II-TM agree for size parameters up to 150, and the comparison gives us confidence in using II-TM as a benchmark for size parameters up to 150 for other geometries (e.g., hexagonal columns) because the applicability of II-TM with respect to particle shape is generic, as demonstrated in our previous studies involving a complex aggregate. This study demonstrates the convergence of the exact II-TM and approximate PGOM solutions for the complete set of single-scattering properties of a nonspherical shape other than spheroids and circular cylinders with particle sizes of $\sim 48\lambda$ (size parameter ~ 150), specifically a hexagonal column with a length size parameter of $kL = 300$, where $k = 2\pi/\lambda$ and L is the column length. IGOM is also quite accurate except near the exact 180° backscattering direction. This study demonstrates that a synergetic combination of the numerically-exact II-TM and the approximate PGOM can seamlessly cover the entire size parameter range of practical interest. To demonstrate the applicability of the approach, we compute the optical properties of dust particles and demonstrate a downstream application to the retrieval of dust aerosol optical thickness and effective particle size from satellite polarimetric observations.

1. INTRODUCTION

The single-scattering properties of nonspherical dielectric particles, namely the single-scattering albedo, the extinction efficiency, and the scattering phase matrix, are important for applications in many disciplines, including atmospheric and oceanic remote sensing [1–5] and bio-optics [6–8]. For practical applications such as remote sensing of clouds and ocean color, it is necessary to consider the particle size distribution rather than to simply assume a monodisperse particle population (i.e., all the particles in the ensemble are assumed to be of the same size). For this reason, size parameters involved in numerical light scattering computation range from the Rayleigh regime in conjunction with small size particles to

Received 28 November 2018, Accepted 16 January 2018, Scheduled 23 January 2019

* Corresponding author: Ping Yang (pyang@tamu.edu).

[1] Department of Atmospheric Sciences, Texas A&M University, College Station, TX 77843, USA. [2] Joint Institute for Regional Earth System Science and Engineering and Department of Atmospheric and Oceanic Sciences, University of California, Los Angeles, CA 90095, USA. [3] Department of Physics & Astronomy and Institute for Quantum Science and Engineering, Texas A&M University, College Station, TX 77843, USA. [4] NASA Goddard Institute for Space Studies, New York, NY 10025, USA.

the geometric optics regime in conjunction with large size particles. Although the research community has expended significant effort on developing numerous methods to compute the optical properties of nonspherical dielectric particles, at present no single method is applicable to particles everywhere in this entire size parameter domain.

With current computational resources, numerical methods for light scattering, such as the finite-difference time-domain (FDTD) method (e.g., [9–14]), the pseudo-spectral time domain (PSTD) method [15, 16], and the discrete dipole approximation (DDA) method (e.g., [17–19]), are usually limited to size parameters smaller than on the order of 50 for practical applications. This is particularly true when the random orientation condition is imposed in the numerical computation, or when repeated simulations are required for a number of particles at multiple wavelengths. However, it is worth noting that PSTD and DDA have been applied to quite large size parameters in special cases, such as applying DDA to an optically tenuous sphere with a size parameter of 160 and an index of refraction of 1.05 [20], and applying PSTD to a sphere with a size parameter of 200 and an index of refraction of $1.312 + i1.489 \times 10^{-9}$ [21]. The T-matrix method [1, 22, 23] is an exact method with the unique ability of averaging the single-scattering properties over random orientations in an analytic form [24]. The T-matrix method has been implemented in terms of the extended boundary condition method (EBCM; e.g., [25–28]), the superposition T-matrix method (STMM; e.g., [29–31]), and the invariant imbedding T-matrix method (II-TM; [32–35]). The EBCM is also referred to as the null-field method [36]. The EBCM is based on electromagnetic surface integral equations and mathematically treats the scattering of light by a particle as a boundary value problem. Unlike EBCM, II-TM stems from an electromagnetic volume integral equation and is numerically implemented as an initial-value problem through an iterative procedure. In terms of solving a differential equation, an initial-value problem is usually easier than a boundary-value problem. In the literature, T-matrix solutions have been reported for some canonical problems involving nonspherical particles with size parameters reaching 150–200, for example, spheroids [33, 37], circular cylinders [38], and hexagonal columns [35], mainly for the phase function and the degree of linear polarization.

The geometric optics method was developed to compute the single-scattering properties of large nonspherical particles (e.g., [39–47]). This method is based on a phenomenological approximation of an electromagnetic wave in terms of a bundle of rays. The conventional geometric optics method computes the scattered field based on the ray-tracing technique. As pointed out by van de Hulst [39], it is not plausible to specify a ray with length L if its cross-sectional dimension is smaller than $\sqrt{L\lambda}$, implying that the ray-tracing technique is not applicable to a particle with a size on the order of the incident wavelength λ or smaller. Although it is generally understood that the ray-tracing technique is applicable only to large particles, the lower limit of the applicable size parameter region has not been clearly determined; such a lower limit in fact depends on whether a differential single-scattering property (e.g., the phase function) or an integral single-scattering property (e.g., the extinction efficiency) is of concern. To compute the complete set of the single-scattering properties of a nonspherical particle with the conventional geometric optics method, it is likely that the size parameter needs to be larger than ~ 200 for reasonable accuracy [35, 38].

Figure 1 schematically depicts the applicable regimes of FDTD, PSTD, DDA, and the conventional geometric optics method for practical applications that may involve an ensemble of randomly oriented particles with various sizes at multiple wavelengths in a wide spectral region. For spheres, the Lorenz—Mie theory [48, 49] can be employed to effectively and efficiently compute the complete set of single-scattering properties. As schematically illustrated by Fig. 1, with the current computing resources there is a gap between the FDTD/PSTD/DDA and the conventional geometric optics method from the point of view of practical light-scattering computations.

Physical-geometric optics methods (PGOMs) based on an electromagnetic surface-integral or volume-integral equation to map the near-field to the far-field have been developed to extend the applicability to smaller size parameters that are infeasible with the conventional geometric optics method (e.g., [50]). It should be pointed out that the idea of mapping the near-field computed with geometric optics principles to the far-field can be traced to the work of Muinonen [51] who used a modified Kirchhoff approximation [52]. However, similar to the case of the conventional geometric optics method, in [51] the contributions by diffraction and geometric rays are separated with equal weights for the extinction cross section based on assuming a constant extinction efficiency ($Q_{ext} = 2$) regardless of particle size.

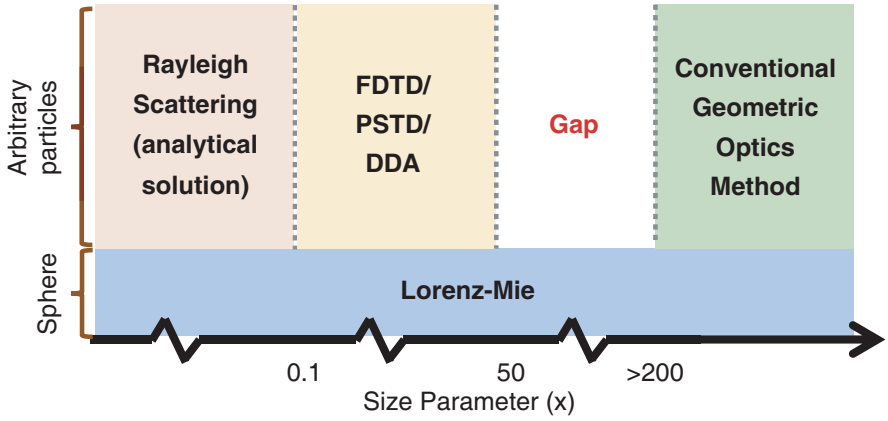

Figure 1. Schematic illustration of the applicable size-parameter regimes of FDTD, PSTD, DDA, and the conventional geometric optics method for arbitrary particle shapes. Note that, in the Rayleigh scattering regime, the single-scattering properties can be analytically solved regardless of the particle shape.

Unlike the conventional geometric optics method, PGOM is able to account for the variation of the extinction efficiency as a function of particle size. In the case of a convex particle, Bi et al. [53] and Sun et al. [54] substantially improved the computational efficiency of PGOM by incorporating some computer graphics techniques into a beam-tracing technique for computing the near-field in PGOM.

In this study, we further improve the previous PGOM algorithm and extend it to more complicated particle geometries such as aggregates. Here we first illustrate the convergence of the exact T-matrix method and PGOM for a canonical case of hexagonal columns with size parameters up to $kL = 300$. Note that the optical properties of hexagonal ice crystal columns and plates, the basic particle habits in cirrus clouds, have been extensively studied because of their importance in climate studies and remote sensing implementations [2, 3, 5, 55–57]. Furthermore, we also illustrate the convergence of II-TM and PGOM for the case of an ice crystal aggregate under the random orientation condition. The convergence of the two methods implies that a synergetic combination of the two methods can be seamlessly applied to nearly the entire size parameter domain covering the Rayleigh regime to the geometric optics regime. In Section 2, we introduce the exact methods used in the study. Section 3 discusses approximate methods. Numerical results and discussions are presented in Section 4. To illustrate the applicability of the present light-scattering formulations, Section 5 presents the simulations of the single-scattering properties of dust particles for an application to the retrieval of dust optical thickness and effective particle size from spaceborne polarimetric observations. Section 6 summarizes the study.

2. EXACT METHODS USED IN THIS STUDY

In the present study, we use the T-matrix approach as a benchmark method to compute the scattering of light by a nonspherical particle. Note that no numerical implementation is actually exact because the infinite series representing the solutions are truncated in some way. Below we briefly describe the physical meaning of the T-matrix and the two specific implementations of the T-matrix method.

2.1. A Brief Summary of the T-Matrix Method

Assume a monochromatic plane electromagnetic wave with the electric field vector given by

$$\mathbf{E}^{inc}(\vec{r}) = \mathbf{E}_0^{inc} \exp\left(ik\hat{k}\cdot\vec{r}\right), \tag{1}$$

where $k = 2\pi/\lambda$ is the modified wave number; λ is the incident wavelength in the nonabsorbing medium surrounding the scattering particle; $\hat{k}$ denotes a unit vector pointing along the wave propagation direction; $\vec{r}$ is the position vector extending from the origin to the observer; and the time-harmonic

factor $\exp(-i\omega t)$ (with ω being the angular frequency and t being time) is hereinafter omitted. Note that this choice of the time-dependence of a harmonic wave leads to a non-negative imaginary part of the index of refraction [58]. Upon the interaction of the incident wave and a scattering particle, the scattered electric field vector is given in the form [39, 58, 59]

$$\mathbf{E}^{sca}(\vec{r}) = \frac{\exp\left[ik(r-\hat{k}\cdot\vec{r})\right]}{-ikr}\mathbf{S}(\hat{r},\hat{k})\mathbf{E}^{inc}, \tag{2a}$$

$$\mathbf{S}(\hat{r},\hat{k}) = \begin{pmatrix} S_2 & S_3 \\ S_4 & S_1 \end{pmatrix}, \tag{2b}$$

where the superscripts "*inc*" and "*sca*" denote the incident and scattered fields respectively; the unit vector $\hat{r}$ indicates the scattering direction; and $\mathbf{S}(\hat{r},\hat{k})$ is the amplitude scattering matrix that is determined by the intrinsic properties of the scattering particle, specifically particle shape, size, and the index of refraction relative to that of the surrounding medium, as well as the scattering configuration (e.g., the azimuthal angle of the scattering plane if the scattering particle does not have axial symmetry about the incident direction). Once the amplitude scattering matrix is obtained, it is straightforward to compute the other single-scattering properties such as the 4×4 phase matrix. Furthermore, the values of the amplitude scattering matrix elements in the exact forward scattering direction contain extinction information, and such an optical relation is usually referred to as the optical theorem [39].

In the T-matrix method, the incident and the scattered fields are expanded using the vector spherical wave functions (VSWFs) as follows [28, 36, 59]:

$$\mathbf{E}^{inc}(\vec{r}) = \sum_{n=1}^{\infty}\sum_{m=-n}^{n}\left[a_{mn}\mathrm{Rg}\mathbf{M}_{nm}(k\vec{r}) + b_{mn}\mathrm{Rg}\mathbf{N}_{nm}(k\vec{r})\right], \tag{3}$$

$$\mathbf{E}^{sca}(\vec{r}) = \sum_{n=1}^{\infty}\sum_{m=-n}^{n}\left[p_{mn}\mathbf{M}_{nm}(k\vec{r}) + q_{mn}\mathbf{N}_{nm}(k\vec{r})\right],\ r>r_c, \tag{4}$$

where r_c is the radius of the smallest circumscribing sphere of the scattering particle, as shown in Fig. 2; Rg$\mathbf{M}$ and Rg$\mathbf{N}$ are regular VSWFs finite at the origin, while $\mathbf{M}$ and $\mathbf{N}$ are outgoing VSWFs proportional to $1/r$ for large r. For practical computation, the expansion series in Eqs. (3) and (4) must be truncated. The transition matrix (T-matrix) links the incident and scattered expansion coefficients in the form

$$\begin{pmatrix} \mathbf{p} \\ \mathbf{q} \end{pmatrix} = \begin{pmatrix} \mathbf{T}^{11} & \mathbf{T}^{12} \\ \mathbf{T}^{21} & \mathbf{T}^{22} \end{pmatrix}\begin{pmatrix} \mathbf{a} \\ \mathbf{b} \end{pmatrix}, \tag{5}$$

where $\mathbf{p}$, $\mathbf{q}$, $\mathbf{a}$, and $\mathbf{b}$ are the matrix notations of the corresponding expansion coefficients in Eqs. (3) and (4). Compared to the amplitude scattering matrix in Eq. (2), the T-matrix not only contains all single-scattering information [59], that is, the extinction matrix and the phase matrix, but also is independent of the direction of the incident and scattered light. In other words, the T-matrix of a particle is a more intrinsic property than its amplitude scattering matrix. As a milestone in light scattering research, Mishchenko (1991) [24] demonstrated that the T-matrix method provides an analytical approach for averaging the single-scattering properties under the random orientation condition. At present, there are three computationally feasible and efficient approaches to implement the T-matrix method: EBCM [23, 26], II-TM [32–35], and STMM [31], of which the first two will be considered below.

2.2. Extended Boundary Condition T-Matrix Method

The EBCM is based on the surface integral equation discussed below. The computation of the T-matrix of a scattering particle in the EBCM is related to the surface integration associated with the particle boundary and the corresponding matrix inversion. When the particle has a large size parameter, or an extreme aspect ratio (the ratio of the minimum characteristic dimension to the maximum characteristic dimension of the particle) implying that the radius of its smallest circumscribing sphere is much larger than the radius of its largest inscribed sphere, the matrix associated with the surface

integration can become ill-conditioned [37]. Consequently, the stability and the convergence rate of the T-matrix computation are substantially degraded as the number of expansion terms in Eqs. (3) and (4) increases. Moreover, the computer CPU cost of the EBCM is significantly affected by the particle morphology. In particular, EBCM is most efficient for homogeneous and layered particles that have rotational symmetries [60], and generally useful for particles with small-to-moderate sizes and with small-to-moderate degrees of nonsphericity or particle aspect ratio. Computations for other geometries (e.g., polyhedral particles) are possible (e.g., [61–63]), which, however, are significantly more involved, particularly for a relatively large size parameter, a significant degree of nonsphericity, or an extreme aspect ratio.

Using the vector Green's theorem, two electromagnetic surface-integral equations for the scattered and incident fields are given in the form [28, 59]

$$\mathbf{E}^{sca}(\vec{r}\,') = \oint_S dS \left\{ ik \left[\hat{n}_s \times \mathbf{H}^{int}(\vec{r})\right] \cdot \overleftrightarrow{G}(\vec{r},\vec{r}\,') + \left[\hat{n}_s \times \mathbf{E}^{int}(\vec{r})\right] \cdot \left[\nabla \times \overleftrightarrow{G}(\vec{r},\vec{r}\,')\right] \right\}, \ \vec{r}\,' \in V_0, \tag{6}$$

$$\mathbf{E}^{inc}(\vec{r}\,') = -\oint_S dS \left\{ ik \left[\hat{n}_s \times \mathbf{H}^{int}(\vec{r})\right] \cdot \overleftrightarrow{G}(\vec{r},\vec{r}\,') + \left[\hat{n}_s \times \mathbf{E}^{int}(\vec{r})\right] \cdot \left[\nabla \times \overleftrightarrow{G}(\vec{r},\vec{r}\,')\right] \right\}, \ \vec{r}\,' \in V_1, \tag{7}$$

where the particle is assumed to be homogeneous; the superscript "*int*" denotes the interior fields; S is the particle surface; V_1 and V_0 are the volume inside and outside the particle, respectively, as shown in Fig. 2; and $\overleftrightarrow{G}$ is the free space dyadic Green's function [64].

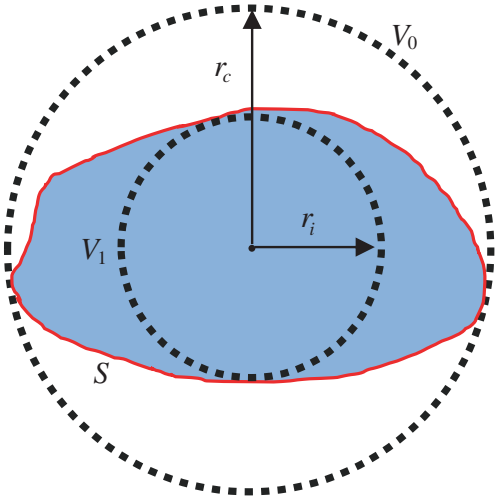

Figure 2. A 2-D schematic diagram illustrating the EBCM T-matrix method. The blue shaded area represents a scattering particle. The red closed curve depicts the surface of the particle S. Two dashed circles represent the largest inscribed sphere and the smallest circumscribing sphere of the particle, respectively, with r_i and r_c being the corresponding radii. V_1 and V_0 are the volumes inside and outside the particle, respectively.

Using VSWFs to expand the fields, the above two equations lead to the relation

$$\begin{pmatrix} \mathbf{p} \\ \mathbf{q} \end{pmatrix} = -\mathrm{Rg}\mathbf{Q} \begin{pmatrix} \mathbf{c} \\ \mathbf{d} \end{pmatrix}, \quad \begin{pmatrix} \mathbf{a} \\ \mathbf{b} \end{pmatrix} = \mathbf{Q} \begin{pmatrix} \mathbf{c} \\ \mathbf{d} \end{pmatrix}, \tag{8}$$

where $(\mathbf{p},\mathbf{q})^T$, $(\mathbf{c},\mathbf{d})^T$, and $(\mathbf{a},\mathbf{b})^T$, where superscript T denotes transpose, are vectors indicating the expansion coefficients of the scattered, interior, and incident fields; the surface integrations are included in $\mathrm{Rg}\mathbf{Q}$ and $\mathbf{Q}$. The explicit expressions of $\mathrm{Rg}\mathbf{Q}$ and $\mathbf{Q}$ are given in [28, 59].

From Eq. (8), the T-matrix can be given by

$$\begin{pmatrix} \mathbf{p} \\ \mathbf{q} \end{pmatrix} = \mathbf{T} \begin{pmatrix} \mathbf{a} \\ \mathbf{b} \end{pmatrix}, \quad \mathbf{T} = -\left(\mathrm{Rg}\mathbf{Q}\right) \mathbf{Q}^{-1}. \tag{9}$$

For a particle with mirror symmetry under the random orientation condition, the scattering phase matrix is given in the form [39, 65, 66]:

$$P(\Theta) = \begin{pmatrix} a_1 & b_1 & 0 & 0 \\ b_1 & a_2 & 0 & 0 \\ 0 & 0 & a_3 & b_2 \\ 0 & 0 & -b_2 & a_4 \end{pmatrix}, \tag{10}$$

where Θ is the scattering angle and is suppressed in the matrix elements. Note that the symmetry relations among the phase matrix elements in the forward and backward scattering directions have been extensively investigated under numerous scenarios [67]. The scattering phase matrix can be analytically given by using the T-matrix of the particle. In particular, the phase function is expanded in terms of the Wigner d-functions as:

$$a_1(\Theta) = \sum_{s=0}^{\infty} \alpha_1^s d_{00}^s(\Theta), \tag{11}$$

where the expansion coefficients are analytically computed using the T-matrix. The asymmetry factor is given by

$$\begin{aligned} g &= \langle \cos\theta \rangle = \frac{1}{2}\int_0^{\pi} \alpha_1(\theta)\cos\theta \sin\theta d\theta. \\ &= \frac{1}{3}\alpha_1^1. \end{aligned} \tag{12}$$

In addition, the extinction and scattering cross-sections in random orientation can be explicitly calculated from T-matrix elements:

$$\langle C_{ext} \rangle = -\frac{2\pi}{k^2} \sum_{n=1}^{\infty} \sum_{m=-n}^{n} \mathrm{Re}\left(T_{mnmn}^{11} + T_{mnmn}^{22}\right), \tag{13}$$

$$\langle C_{sca} \rangle = \frac{2\pi}{k^2} \sum_{n=1}^{\infty} \sum_{m=-n}^{n} \sum_{n'=1}^{\infty} \sum_{m'=-n'}^{n'} \left[\left|T_{mnm'n'}^{11}\right|^2 + \left|T_{mnm'n'}^{12}\right|^2 + \left|T_{mnm'n'}^{21}\right|^2 + \left|T_{mnm'n'}^{22}\right|^2 \right], \tag{14}$$

where the symbol $\langle\,\rangle$ indicates an averaged quantity under the random orientation condition.

2.3. Invariant-Imbedding T-Matrix Method

The II-TM method is based on the electromagnetic volume integral equation. The volume integral equation can be written using the dyadic Green's function as follows [59]:

$$\mathbf{E}(\vec{r}) = \mathbf{E}^{inc}(\vec{r}) + k^2 \iiint_V \left[m^2(\vec{r}\,') - 1\right] \overleftrightarrow{G}(\vec{r}, \vec{r}\,') \cdot \mathbf{E}(\vec{r}\,') d^3\vec{r}\,', \tag{15}$$

where V represents the volume whose refractive index is not the same as that of the surrounding medium; m is the relative refractive index; and the free space dyadic Green's function satisfies the following equation:

$$\nabla \times \nabla \times \overleftrightarrow{G}(\vec{r}, \vec{r}\,') - k^2 \overleftrightarrow{G}(\vec{r}, \vec{r}\,') = \overleftrightarrow{I}\delta(\vec{r} - \vec{r}\,'). \tag{16}$$

Here $\overleftrightarrow{I}$ is the unit dyadic, and the dyadic Green's function can also be expanded in terms of the VSWFs [68]. Using Eq. (15) and the invariant-imbedding technique, the T-matrix in II-TM can be formally written as [32, 33, 35]:

$$\mathbf{T}(r_n) = \mathbf{Q}_{jj}(r_n) + \left[\mathbf{I} + \mathbf{Q}_{jh}(r_n)\right] \left[\mathbf{I} - \mathbf{T}(r_{n-1})\mathbf{Q}_{hh}(r_n)\right]^{-1} \mathbf{T}(r_{n-1}) \left[\mathbf{I} + \mathbf{Q}_{hj}(r_n)\right], \tag{17}$$

where all $\mathbf{Q}$ terms are super matrices (i.e., each element of $\mathbf{Q}$ is also a matrix) and are related to a spherical shell integration or a solid angle integration, and the matrices only depend on the layer n. All

of the **Q** terms contain a U-matrix element that is the only term dependent on the particle shape and refractive index in the II-TM formulation. An arbitrary element of the U-matrix is [35]

$$U_{iji'j'}(r) = \frac{k^2 r^2}{4\pi} \int_0^{2\pi} d\varphi \int_0^{\pi} d\theta \sin\theta e^{-i(j-j')\varphi} \times (m^2-1) K_{iji'j'}(r,\theta,\varphi), \tag{18}$$

where $K_{iji'j'}$ is a 3×3 matrix that contains spherical wave functions [35]. The integration in Eq. (18) is on a sphere with radius r.

II-TM is implemented by proceeding from the innermost core to the outermost layer. The innermost core is a homogeneous sphere, whose T-matrix is given by the Lorenz—Mie coefficients. The T-matrix of any outer layer n can be computed using the T-matrix of layer $n-1$ and quantities related only to the morphology of layer n. When the iteratively computational procedure is completed for the smallest circumscribed sphere, the corresponding solution is the T-matrix for the scattering particle. An illustrative schematic of II-TM is shown in Fig. 3. The physical meaning of Eq. (17) is that the T-matrix in layer r_{p+1} can be obtained using the T-matrix in layer r_p and a matrix Q related to the refractive index of layer r_{p+1}. The final T-matrix is then recursively obtained.

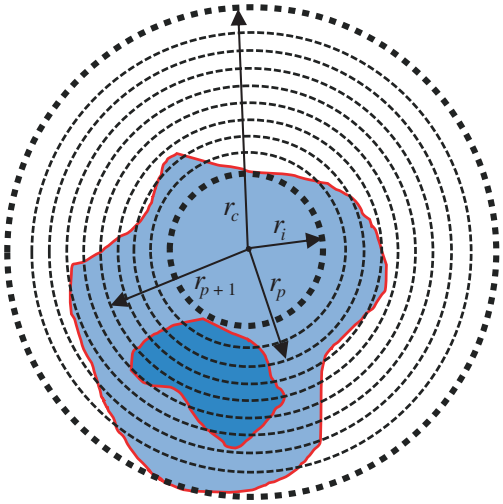

Figure 3. A 2-D schematic diagram illustrating the II-TM method. The shaded area represents an inhomogeneous scattering particle. The two red closed curves depict the boundaries of two parts of the particle. The two thick dashed circles represent the largest inscribed sphere and the smallest circumscribing sphere of the particle, respectively, with r_i and r_c being the corresponding radii. The thin dashed circles represent intermediate radii used in the iterative II-TM method; r_p and r_{p+1} denote successive radii.

The function on the right-hand-side of Eq. (17) includes integration over an inhomogeneous spherical shell (with a portion occupied by the particle and the remaining portion of the surrounding medium) and matrix inversions. All matrices are well-conditioned in the imbedding process. Moreover, II-TM is exceptionally stable even if the scattering particle has an extreme shape, such as for large size parameters, extreme aspect ratios, or complex morphologies.

3. APPROXIMATE METHODS USED IN THIS STUDY

When a nonspherical scattering particle corresponds to a sufficiently large size parameter, the geometric optics method seems to be the only choice in practice. Rigorous ray-tracing involving curved particle surface is quite complicated [45, 46, 69, 70]. Here we only consider faceted particles for which all the rays incident on the same surface are coherent. In the near field, the ray-tracing process can be efficiently implemented in terms of a broad-beam tracing technique [53, 54]. In the far field, the surface or volume

integral equations (Eqs. (6) and (15)) derived from Maxwell's equations can be employed to map the near field to the far field.

The explicit solution of Eq. (16) is (e.g., [59])

$$\overleftrightarrow{G}\left(\vec{r},\vec{r}\,'\right)=\left(\overleftrightarrow{I}+\frac{1}{k^2}\nabla\otimes\nabla\right)\frac{\exp\left(ik\left|\vec{r}-\vec{r}\,'\right|\right)}{4\pi\left|\vec{r}-\vec{r}\,'\right|}, \tag{19}$$

where '$\otimes$' is the outer product symbol. For two vectors, $\mathbf{A}=(a_1,a_2,a_3)$ and $\mathbf{B}=(b_1,b_2,b_3)$, the outer product is defined in the form

$$\mathbf{A}\otimes\mathbf{B}=\begin{pmatrix} a_1b_1 & a_1b_2 & a_1b_3 \\ a_2b_1 & a_2b_2 & a_2b_3 \\ a_3b_1 & a_3b_2 & a_3b_3 \end{pmatrix}. \tag{20}$$

In the far field approximation when $kr\rightarrow\infty$, Eq. (19) can be written as (e.g., [59])

$$\overleftrightarrow{G}\left(\vec{r},\vec{r}\,'\right)\approx\left(\overleftrightarrow{I}-\hat{r}\otimes\hat{r}\right)\frac{\exp\left[ik\left(r-\hat{r}\cdot\vec{r}\,'\right)\right]}{4\pi r}, \tag{21}$$

where $r=|\vec{r}|$, and $\hat{r}=\vec{r}/r$. Substituting Eq. (21) into Eqs. (6) and (15), the surface and volume integral equations in the far field can be written as [47, 50, 59 and references cited therein]:

$$\mathbf{E}^{sca}(\vec{r})|_{kr\rightarrow\infty}=\frac{\exp(ikr)}{-ikr}\frac{k^2}{4\pi}\hat{r}\times\oiint_S\left\{\hat{n}_s\times\mathbf{E}(\vec{r}\,')-\hat{r}\times\left[\hat{n}_s\times\mathbf{H}(\vec{r}\,')\right]\right\}\exp(-ik\hat{r}\cdot\vec{r}\,')d^2\vec{r}\,', \tag{22}$$

$$\mathbf{E}^{sca}(\vec{r})|_{kr\rightarrow\infty}=\frac{\exp(ikr)}{-ikr}\frac{ik^3}{4\pi}\iiint_V\left(1-m^2\right)\left[\mathbf{E}(\vec{r}\,')-\hat{r}\cdot\mathbf{E}(\vec{r}\,')\right]\exp(-ik\hat{r}\cdot\vec{r}\,')d^3\vec{r}\,'. \tag{23}$$

Either of the above two equations can be used to obtain the far field once the near electromagnetic field is obtained by the geometric optics method. The near-to-far field mapping uses the surface- or volume-integral equation and accurately represents the approximations of physical optics. The preceding mapping of the near-field to the far-field, an idea originally developed by Yang and Liou [47, 50], is the basis of PGOM.

To show the equivalence of Eqs. (22) and (23), we consider Maxwell's equations in Gaussian units for a time-harmonic field in a medium, given by

$$\nabla\cdot\mathbf{E}(\vec{r})=0,\quad\nabla\times\mathbf{E}(\vec{r})=i\mu_rk_0\mathbf{H}(\vec{r}), \tag{24}$$

$$\nabla\cdot\mathbf{H}(\vec{r})=0,\quad\nabla\times\mathbf{H}(\vec{r})=-i\varepsilon_rk_0\mathbf{E}(\vec{r}), \tag{25}$$

where k_0 is the wave number of the field in vacuum, and μ_r and ε_r are the relative permeability and permittivity, respectively. Here light scattering by a non-magnetic dielectric particle in a non-magnetic medium is considered, and thus we can assume $\mu_r=1$. Consequently, the modified wave number in the medium is defined as

$$k=\sqrt{\varepsilon_r}k_0. \tag{26}$$

The modified wave numbers associated with the scattering medium and the surrounding medium are denoted as k_1 and k, and the corresponding permittivities are denoted as ε_{r_1} and ε_r. Using Maxwell's equations and the vector Green's theorem, the surface-integral equation and the volume-integral equation for the electric field can be rewritten as (e.g., [28, 59, 71]):

$$\mathbf{E}(\vec{r})=\mathbf{E}^{inc}(\vec{r})+\oiint_S d^2\vec{r}\,'\left\{ik_0\left[\hat{n}_s\times\mathbf{H}(\vec{r}\,')\right]\cdot\overleftrightarrow{G}(\vec{r}\,',\vec{r})+\left[\hat{n}_s\times\mathbf{E}(\vec{r}\,')\right]\cdot\left[\nabla'\times\overleftrightarrow{G}(\vec{r}\,',\vec{r})\right]\right\}, \tag{27}$$

$$\mathbf{E}(\vec{r})=\mathbf{E}^{inc}(\vec{r})+k^2\iiint_V\left(m^2-1\right)\overleftrightarrow{G}(\vec{r},\vec{r}\,')\cdot\mathbf{E}(\vec{r}\,')d^3\vec{r}\,', \tag{28}$$

where the field point $\vec{r}$ is outside the scattering particle and $m^2=\varepsilon_{r_1}/\varepsilon_r=k_1^2/k^2$.

Starting from the scattering field in the volume-integral equation, Eq. (28),

$$k^2\iiint_V\left(m^2-1\right)\overleftrightarrow{G}(\vec{r},\vec{r}\,')\cdot\mathbf{E}(\vec{r}\,')d^3\vec{r}\,'=\iiint_V\left(k_1^2-k^2\right)\mathbf{E}(\vec{r}\,')\cdot\overleftrightarrow{G}(\vec{r}\,',\vec{r})d^3\vec{r}\,', \tag{29}$$

where the symmetry relation $\overleftrightarrow{G}^T(\vec{r}',\vec{r}) = \overleftrightarrow{G}(\vec{r},\vec{r}')$ is used. Substituting Eq. (16) into Eq. (29), we obtain

$$\iiint_V \left[k_1^2\mathbf{E}(\vec{r}')\cdot\overleftrightarrow{G}(\vec{r}',\vec{r}) - \mathbf{E}(\vec{r}')\cdot\nabla'\times\nabla'\times\overleftrightarrow{G}(\vec{r}',\vec{r}) + \mathbf{E}(\vec{r}')\overleftrightarrow{I}\delta\left(\vec{r}'-\vec{r}\right)\right]d^3\vec{r}'. \tag{30}$$

Because $\vec{r}'$ and $\vec{r}$ are inside and outside of the scattering medium, respectively, the Dirac delta function term in Eq. (30) vanishes. Combining the two curl functions in Eqs. (24) and (25), we have

$$\nabla'\times\nabla'\times\mathbf{E}(\vec{r}') - k_1^2\mathbf{E}(\vec{r}') = 0. \tag{31}$$

Substituting Eq. (31) into Eq. (30), we obtain

$$\iiint_V \left[\nabla'\times\nabla'\times\mathbf{E}(\vec{r}')\cdot\overleftrightarrow{G}(\vec{r}',\vec{r}) - \mathbf{E}(\vec{r}')\cdot\nabla'\times\nabla'\times\overleftrightarrow{G}(\vec{r}',\vec{r})\right]d^3\vec{r}'. \tag{32}$$

Using the vector Green's theorem, we obtain

$$\begin{aligned}
&\iiint_V \left[\nabla'\times\nabla'\times\mathbf{E}(\vec{r}')\cdot\overleftrightarrow{G}(\vec{r}',\vec{r}) - \mathbf{E}(\vec{r}')\cdot\nabla'\times\nabla'\times\overleftrightarrow{G}(\vec{r}',\vec{r})\right]d^3\vec{r}' \\
&= \oiint_S d^2\vec{r}'\hat{n}_s\cdot\left\{\mathbf{E}(\vec{r}')\times\left[\nabla'\times\overleftrightarrow{G}(\vec{r}',\vec{r})\right] - \overleftrightarrow{G}(\vec{r}',\vec{r})\times\left[\nabla'\times\mathbf{E}(\vec{r}')\right]\right\} \\
&= \oiint_S d^2\vec{r}'\left\{\left[\hat{n}_s\times\mathbf{E}(\vec{r}')\right]\cdot\left[\nabla'\times\overleftrightarrow{G}(\vec{r}',\vec{r})\right] + \hat{n}_s\times\left[\nabla'\times\mathbf{E}(\vec{r}')\right]\cdot\overleftrightarrow{G}(\vec{r}',\vec{r})\right\} \\
&= \oiint_S d^2\vec{r}'\left\{ik_0\left[\hat{n}_s\times\mathbf{H}(\vec{r}')\right]\cdot\overleftrightarrow{G}(\vec{r}',\vec{r}) + \left[\hat{n}_s\times\mathbf{E}(\vec{r}')\right]\cdot\left[\nabla'\times\overleftrightarrow{G}(\vec{r}',\vec{r})\right]\right\}
\end{aligned} \tag{33}$$

in which the curl equation in Eq. (24) is used for the last step of the derivation. Thus, the volume-integral equation and the surface-integral equation are proven to be equivalent.

The integrals over surface S or volume V in Eqs. (22) and (23) can be decomposed into surface or volume elements based on the order of a geometric optical ray, for example, external reflection, refraction without internal reflection, refraction with one internal reflection, and so on. These element integrals can be analytically obtained for a faceted particle. However, when a beam is incident on multiple facets in the next scattering order, a beam-splitting algorithm is necessary to ensure that each split beam is only incident on a specific facet. The beam-splitting process is accomplished using a computer graphics technique. The technique ensures the most efficient splitting so that the beam number is significantly reduced [54].

In previous studies [53, 54], the ray-tracing and beam clipping techniques are applied only to single convex faceted particles. In the current study, we extend the technique to deal with concave faceted particles. For concave particles, we trace not only the beams within the particle but also the beams propagating outside the particle, because the beams may re-enter the particle. In the implementation of the ray-tracing process, it is necessary to determine if the beam would propagate to a specific facet, and if the beam is blocked by other parts of the particle. A beam may propagate to more than one facet, so we need to split the beam into several sub-beams.

We develop a beam splitting algorithm illustrated in Fig. 4 to find the facets that a beam propagates to, and the shape of each sub-beam. To determine if a beam impinges on a facet, the first step is to determine if the beam intersects with a plane coinciding with the facet. If the beam intersects with the plane, we obtain the 2D projections of the beam and the facet on the aforesaid plane. The two projections are two polygons. Then we determine if the two polygons intersect with each other. If their projections intersect, the beam can impinge on the facet. However, because the particle may be concave, the propagation route may be blocked by facets of the particle, as illustrated in Fig. 5. Furthermore, it is necessary to determine if the beam impinges on other facets before reaching the targeted facet. If this is the case, the blocked portion of the beam is not further considered.

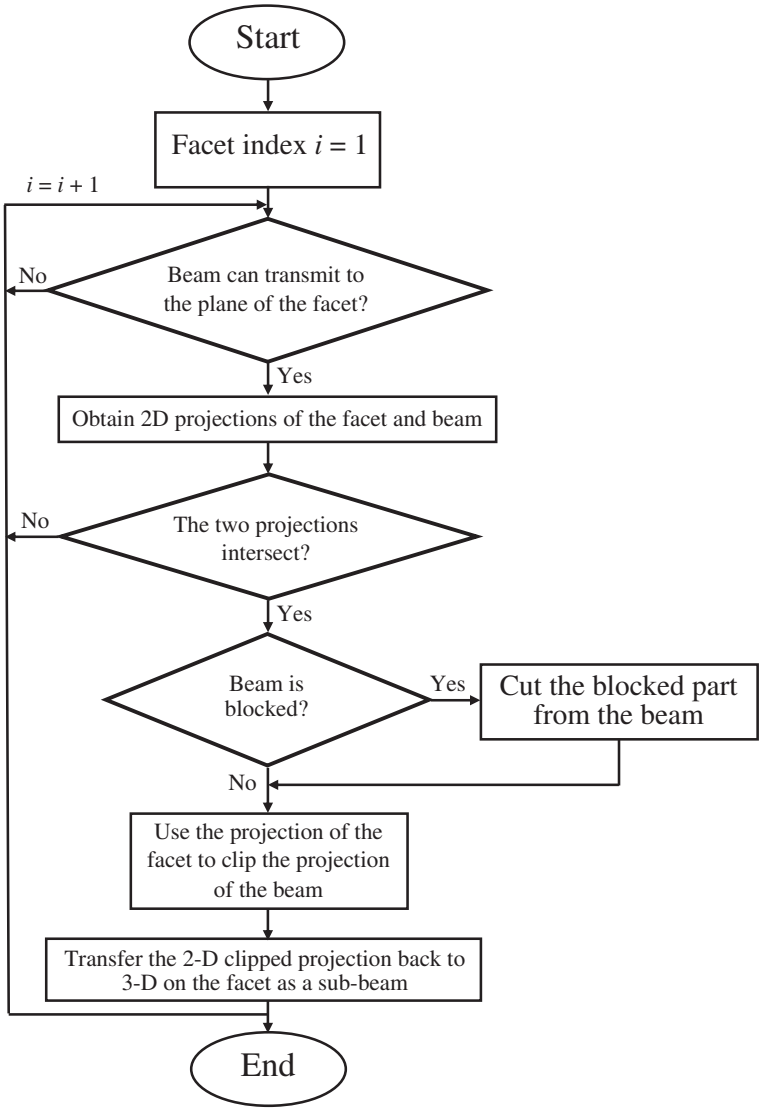

Figure 4. Flowchart of beam splitting process.

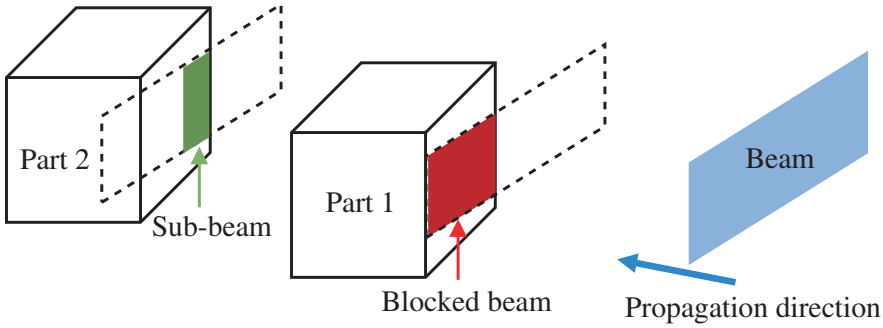

Figure 5. An illustration of beam splitting among different parts of a particle. In this illustration, the facet facing the beam on Part 2 is the targeted facet. Part of the beam is blocked by Part 1. The dashed frames show the shapes of the propagating beam, if it does not encounter any obstacles.

Next, we use a polygon-clipping algorithm to obtain the overlapping polygon of the projections of the facet and the beam, and transfer the overlapping polygon to a 3D polygon on the plane coinciding with the facet. The overlapping 3D polygon is the sub-beam from the original beam impinging on the facet. To effectively implement the beam splitting algorithm mentioned above, an efficient 2-D polygon-clipping algorithm is necessary. Here we adopt the Weiler-Atherton algorithm [72] used in [54] to implement clipping between two polygons.

Particle extinction, scattering, and absorption efficiencies are three important parameters to measure the scattering properties of a particle. To obtain the three parameters, it is necessary to know the projected area of the particle in addition to the extinction, scattering, and absorption cross sections. The projection of a convex particle is a convex polygon and it is straightforward to compute its area. The random orientation-averaged projected area is a quarter of its surface area [73, 74]. However, the projection of a concave particle may or may not be a concave polygon. Its random-orientation-averaged projected area is computed by numerically averaging projected areas for many different orientations. In a previous study [75], a Monte Carlo method was developed to compute the projected area of a concave particle in a specific orientation. Here we develop an analytical method to compute the projected area of a concave particle, which is presented in detail in the appendix.

The analytical volume element integral expressions have been given in [53, 54]. Here we present an expression of the surface element integral. In Eq. (22), the electric field $\mathbf{E}$ and magnetic field $\mathbf{H}$ in Gaussian units are related by

$$\mathbf{H} = \hat{e} \times \mathbf{E}, \tag{34}$$

where $\hat{e}$ is the propagation direction. Thus, we only need to consider the electric field in the ray-tracing process. We can separate the transverse electric field into two orthogonal polarization directions. One is perpendicular to the scattering plane (β direction) and the other is in the scattering plane (α direction). The incident, scattered, and near electric fields can be written as

$$\mathbf{E}^{sca} = E_{\alpha}^{sca}\hat{\alpha}^{sca} + E_{\beta}^{sca}\hat{\beta}^{sca}, \tag{35a}$$

$$\mathbf{E}^{inc} = E_{\alpha}^{inc}\hat{\alpha}^{inc} + E_{\beta}^{inc}\hat{\beta}^{inc}, \tag{35b}$$

$$\mathbf{E}_p = E_{p,\alpha}\hat{\alpha}_p + E_{p,\beta}\hat{\beta}_p, \tag{35c}$$

where the subscript p represents the reflection order in the ray-tracing process. Substituting Eq. (35) into Eq. (22) and using the relation

$$\hat{r} = \hat{\beta}^{sca} \times \hat{\alpha}^{sca}, \tag{36}$$

we obtain

$$\begin{pmatrix} E_{\alpha}^{sca}(\hat{r}) \\ E_{\beta}^{sca}(\hat{r}) \end{pmatrix} = \frac{ik\exp(ikr)}{4\pi r} \sum_{p=1}^{\infty} \iint\limits_{S_p} \mathbf{L}_p \begin{pmatrix} E_{p,\alpha}(\vec{r}') \\ E_{p,\beta}(\vec{r}') \end{pmatrix} \exp\left(-ik\hat{r}\cdot\vec{r}'\right) d^2\vec{r}', \tag{37}$$

in which matrix $\mathbf{L}_p$ describes the transformation of the electric field reference frame from the pth-order reflection/refraction plane to the incident-scattering plane, and is defined as

$$\mathbf{L}_p = \begin{pmatrix} \hat{n}_{s,p}\cdot\left(\hat{\alpha}_p \times \hat{\beta}^{sca} - \hat{\beta}_p \times \hat{\alpha}^{sca}\right) & \hat{n}_{s,p}\cdot\left(\hat{\beta}_p \times \hat{\beta}^{sca} + \hat{\alpha}_p \times \hat{\alpha}^{sca}\right) \\ -\hat{n}_{s,p}\cdot\left(\hat{\beta}_p \times \hat{\beta}^{sca} + \hat{\alpha}_p \times \hat{\alpha}^{\mathrm{sca}}\right) & \hat{n}_{s,p}\cdot\left(\hat{\alpha}_p \times \hat{\beta}^{sca} - \hat{\beta}_p \times \hat{\alpha}^{sca}\right) \end{pmatrix}, \tag{38}$$

in which $\hat{n}_{s,p}$ denotes the normal direction for the p-th order beam. Eq. (37) suggests that the far field is the sum of the surface integrals of all orders of rays on the outer surface of the particle including the incident field, externally reflected field, and refracted field emerging from the particle. The incident, externally reflected, and refracted fields can be written as

$$\begin{pmatrix} E_{\alpha,1}^{i} \\ E_{\beta,1}^{i} \end{pmatrix} = \mathbf{U}_1^{i} \begin{pmatrix} E_{\alpha}^{inc} \\ E_{\beta}^{inc} \end{pmatrix} \exp\left(ik\delta_{1,1}\right), \tag{39a}$$

$$\begin{pmatrix} E_{\alpha,1}^{R} \\ E_{\beta,1}^{R} \end{pmatrix} = \mathbf{U}_1^{R} \begin{pmatrix} E_{\alpha}^{inc} \\ E_{\beta}^{inc} \end{pmatrix} \exp\left(ik\delta_{1,1}\right), \tag{39b}$$

$$\begin{pmatrix} E_{p,\alpha}(\vec{r}\,') \\ E_{p,\beta}(\vec{r}\,') \end{pmatrix} = \mathbf{U}_p^T \begin{pmatrix} E_\alpha^{inc} \\ E_\beta^{inc} \end{pmatrix} \exp\left[ik\left(N_r \hat{e}_p \cdot \vec{w}_p + \delta_{p,1}\right)\right] \exp\left[-k\left(N_i \vec{\vec{A}}_p \cdot \vec{w}_p + d_{p,1}\right)\right], \; p \geq 2, \quad (39c)$$

in which the $\mathbf{U}$ matrices represent refraction and reflection processes, and related coordinate transformations. $\mathbf{U}_1^i$ is for the incident field, $\mathbf{U}_1^R$ is for the externally reflected field, and $\mathbf{U}_p^T$ describes the refracted field. The explicit forms of these matrices are given in [47]. N is the effective refractive index $N_r + iN_i$ [76], $\delta_{p,1}$ and $d_{p,1}$ are the phase and attenuation factor of the p-th order beam at the first vertex respectively, $\vec{w}_p$ is a position vector on the p-th beam facet starting from the first vertex, and $\hat{e}_p$ and $\vec{\vec{A}}_p$ are perpendicular to the constant phase and constant amplitude plane of the beam respectively. The recursion relations of the quantities are given in [53, 54].

Substituting Eq. (39) into Eq. (37), we obtain

$$\begin{pmatrix} E_\alpha^{sca}(\hat{r}) \\ E_\beta^{sca}(\hat{r}) \end{pmatrix} = \frac{\exp(ikr)}{-ikr} \sum_{p=1}^{\infty} \mathbf{L}_p \mathbf{U}_p \exp\left(ik\delta_{p,1} - kd_{p,1}\right) D_p \begin{pmatrix} E_\alpha^{inc} \\ E_\beta^{inc} \end{pmatrix}, \quad (40)$$

in which D_p is given by

$$D_p = \exp\left(-ik\hat{r} \cdot \vec{r}_{p,1}\right) \frac{k^2}{4\pi} \iint_{s_p} \exp\left[ik\left(N_r \hat{e}_p - \hat{r} + iN_i \vec{\vec{A}}_p\right) \cdot \vec{w}_p\right] d^2\vec{w}_p, \quad (41)$$

where the surface integration area s_p is the beam facet. The analytical form of the D_p integral is

$$D_p = \exp\left(-ik\hat{r} \cdot \vec{r}_{p,1}\right) \frac{k^2}{4\pi} \sum_{j=1}^{n_v} \frac{\left(N_r \hat{e}_p - \hat{r} + iN_i \vec{\vec{A}}_p\right) \times \hat{n}_p \cdot \left(\vec{r}_{p,j+1} - \vec{r}_{p,j}\right)}{\left|N_r \hat{e}_p - \hat{r} + iN_i \vec{\vec{A}}_p\right|^2 - \left[\left(N_r \hat{e}_p - \hat{r} + iN_i \vec{\vec{A}}_p\right) \cdot \hat{n}_p\right]^2}$$
$$\times \frac{\exp\left[ik\left(N_r \hat{e}_p - \hat{r} + iN_i \vec{\vec{A}}_p\right) \cdot \left(\vec{r}_{p,j+1} - \vec{r}_{p,1}\right)\right] - \exp\left[ik\left(N_r \hat{e}_p - \hat{r} + iN_i \vec{\vec{A}}_p\right) \cdot \left(\vec{r}_{p,j} - \vec{r}_{p,1}\right)\right]}{ik\left(N_r \hat{e}_p - \hat{r} + iN_i \vec{\vec{A}}_p\right) \cdot \left(\vec{r}_{p,j+1} - \vec{r}_{p,j}\right)} \quad (42)$$

in which n_v is the number of vertices of the beam facet.

Comparing Eq. (40) and Eq. (2), we obtain the amplitude scattering matrix within the PGOM framework in the form

$$\mathbf{S} = \left(\mathbf{L}^i \mathbf{U}_1 + \mathbf{L}_1 \mathbf{U}_1^R\right) \Gamma \exp\left(ik\delta_{1,1}\right) D_1 + \sum_{p=2}^{\infty} \mathbf{L}_p \mathbf{U}_p^T \Gamma \exp\left(ik\delta_{p,1} - kd_{p,1}\right) D_p, \quad (43)$$

in which matrix Γ describes the electric field reference plane transformation from the incident plane to the scattering plane. The first term on the right-hand side of Eq. (43) represents the contributions from diffraction and external reflection. The second term represents the contributions from the first order refraction and higher order refractions after internal reflections.

The surface integral equation, Eq. (22), indicates that the electromagnetic field considered in the computation is on a closed and connected surface outside the particle. For a convex particle, the closed and connected surface can be the surface of the particle. The surface of a concave particle may not be closed or connected. We thus define a rectangular box enclosing the particle as shown in Fig. 6, and only consider the electromagnetic field on the rectangular faces when computing Eq. (43). The box is fixed relative to the particle, that is, the box and the particle rotate together when different orientations of the particle with respect to the incident direction are considered. To minimize errors when tracing beams on the box surface (note that the accuracy of defining a beam degrades with an increase in its propagation distance), the six faces of the box are set to be as close as possible to the particle but do not intersect with the particle.

The scattered field is the sum of the diffracted field, and the field reflected and refracted by the particle. In addition to the contributions by reflection and refraction, the field on the projected area (i.e., the shadow of the particle) on the enclosing box contains an extra term referred to as the compensating field [77], given by

$$\vec{\vec{E}}_c(\vec{r}) = -\vec{\vec{E}}_i(\vec{r}), \;\; \vec{r} \in \text{the particle shadow}, \quad (44)$$

where the subscripts c and i indicate the compensating and incident fields, respectively. The compensating field leads to a diffracted field in the far-field zone, which is not exactly the same as the diffraction by the particle [78]. Only when the boundary of the illuminated portion of the particle is on the same plane perpendicular to the incident direction, are the diffractions by the particle and the counterpart associated with the compensating field equivalent [78]. For the reflected and refracted fields, the integration areas are the beam projections on the rectangle surface in Fig. 6. Although the diffracted field is not exactly the diffraction of the particle, the total scattered field mapped from the near-field counterpart on the box surfaces is the correct scattered field, because the computation is consistent with the surface integral equation, Eq. (22).

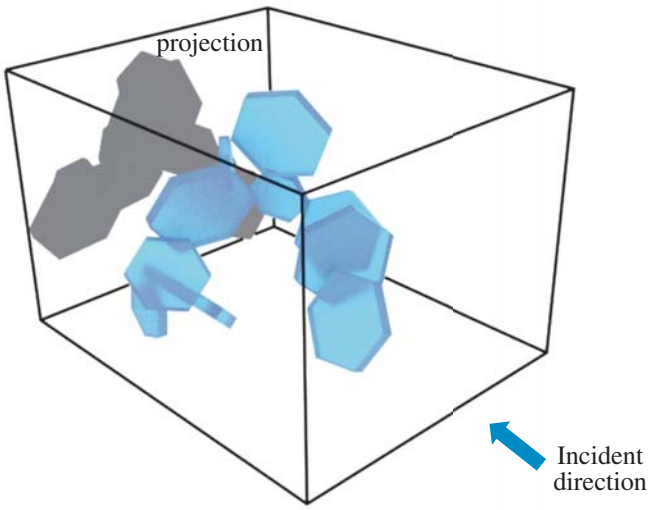

Figure 6. Illustration of surface-integral equation computational region.

4. NUMERICAL RESULTS AND DISCUSSION

4.1. Comparison between II-TM and EBCM for a Size Parameter of 150

Bi et al. [33] compared the two exact methods, EBCM and II-TM, for spheroids with size parameters less than 100. To use II-TM as a benchmark for particles with large size parameters and a more complicated particle geometry, here we will first compare EBCM with the computational program developed by Mishchenko and Travis [26] and the II-TM computational program reported in [33, 35] for computing the scattering properties of a randomly oriented prolate spheroid with an aspect ratio of 1.5 (the ratio of major axis to minor axis). The major axis of the spheroid corresponds to size parameter 150.

Table 1 lists the extinction efficiency (Q_e), single-scattering albedo (SSA), and asymmetry factor (g) computed by II-TM and EBCM. The refractive indices used in the computations are $1.308 + i1.43 \times 10^{-9}$ and $1.2762 + i0.4133$, corresponding to ice refractive indices at wavelengths 0.65 µm and 12 µm, respectively. As can be seen from Table 1, the II-TM results are consistent with the EBCM results to 3 or 4 significant digits.

Figures 7 and 8 show the scattering phase matrix elements of the spheroid computed by II-TM and EBCM. In Fig. 7, the prolate spheroid has refractive index $1.308 + i1.43 \times 10^{-9}$ (the 0.65 µm visible wavelength case). The II-TM and EBCM solutions for the nonzero phase matrix elements are nearly identical. Because the particle is almost nonabsorbing, its phase matrix displays oscillations. Only minor differences between the II-TM and EBCM results can be seen in these oscillations. In Fig. 8, the refractive index is $1.2762 + i0.4133$ (the 12.0 µm infrared wavelength case) where the particle is strongly absorptive. The phase matrix is much smoother than in the nonabsorptive case. The difference between II-TM and EBCM results is hardly seen in Fig. 8.

Table 1. Comparison of Q_e, SSA, and g computed by II-TM and EBCM for randomly oriented prolate spheroids with aspect ratio 1.5 and major axis size parameter 150.

	Q_e (0.65 μm)	SSA (0.65 μm)	g (0.65 μm)	Q_e (12 μm)	SSA (12 μm)	g (12 μm)
II-TM	2.0917	0.9999	0.8514	2.0744	0.5512	0.9444
EBCM	2.0925	0.9998	0.8514	2.0745	0.5516	0.9437

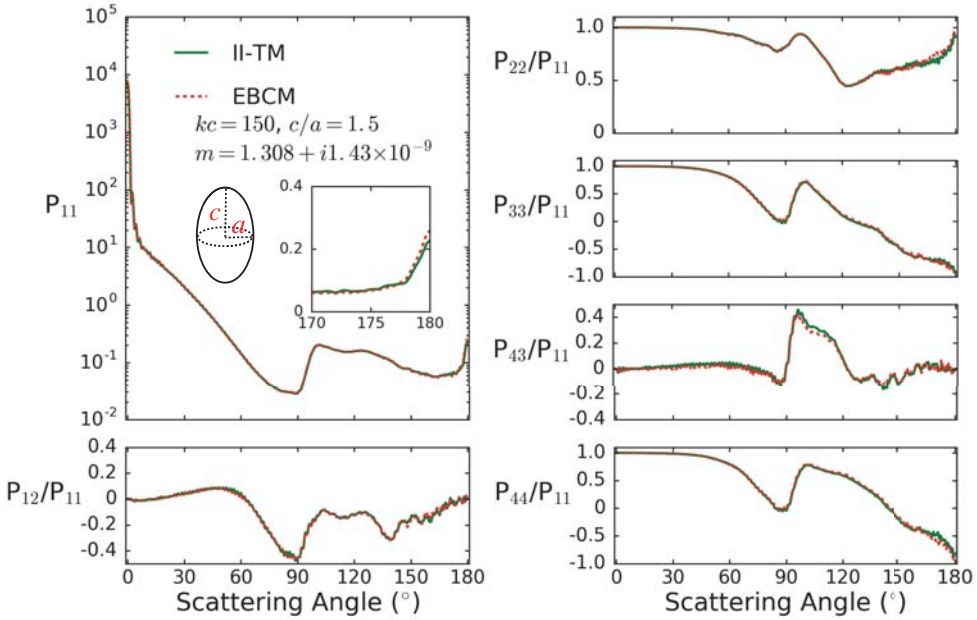

Figure 7. Comparison of the phase matrix elements computed by EBCM and II-TM. The particle is a prolate spheroid with aspect ratio (c/a) 1.5. The major axis size parameter is 150. The refractive index is $1.308 + i1.43 \times 10^{-9}$, which is the ice refractive index at wavelength 0.65 μm. The inset plot shows the P_{11} element for scattering angles 170°–180°.

Previous studies have comprehensively tested the accuracy and convergence of EBCM in computing the single-scattering properties of spheroidal particles (e.g., [37]). Our validation shows excellent consistency between II-TM and EBCM even for size parameters up to 150. This gives us confidence in using II-TM as a benchmark to compare with the approximate geometric-optics methods. It is worth noting that, in principle, numerical implementation of II-TM has no preferential particle geometry except that the computational speed of II-TM for axially symmetric particles is much faster than for nonsymmetric particles. Furthermore, Bi and Yang [35] show excellent agreement between II-TM and DDA phase matrix elements for randomly oriented complex aggregates consisting of ice columns.

4.2. PGOM and II-TM Comparison

Equations (29)–(33) prove that the electromagnetic surface and volume integral equations are equivalent. Here we compare PGOM computations based on both surface and volume integral equations. Figs. 9 and 10 show a comparison between the scattering phase matrices computed by the surface-integral PGOM (PGOMS) and the volume-integral PGOM (PGOMV). The scattering particle is a hexagonal ice column with a unit aspect ratio ($2a/L = 1$). As shown in Fig. 9, the hexagonal column aspect ratio is defined as $2a/L$ where a is the side length of the hexagon, and L is the height of the column. The size parameter (kL) in the calculations is 300. Figs. 9 and 10 show the scattering phase matrices at wavelengths 0.65 μm and 12 μm, respectively. The PGOMS and PGOMV results are consistent.

Both theory and numerical results suggest that PGOMS and PGOMV are equivalent. Thus, we do not include PGOMV in later comparisons between the approximate methods and II-TM.

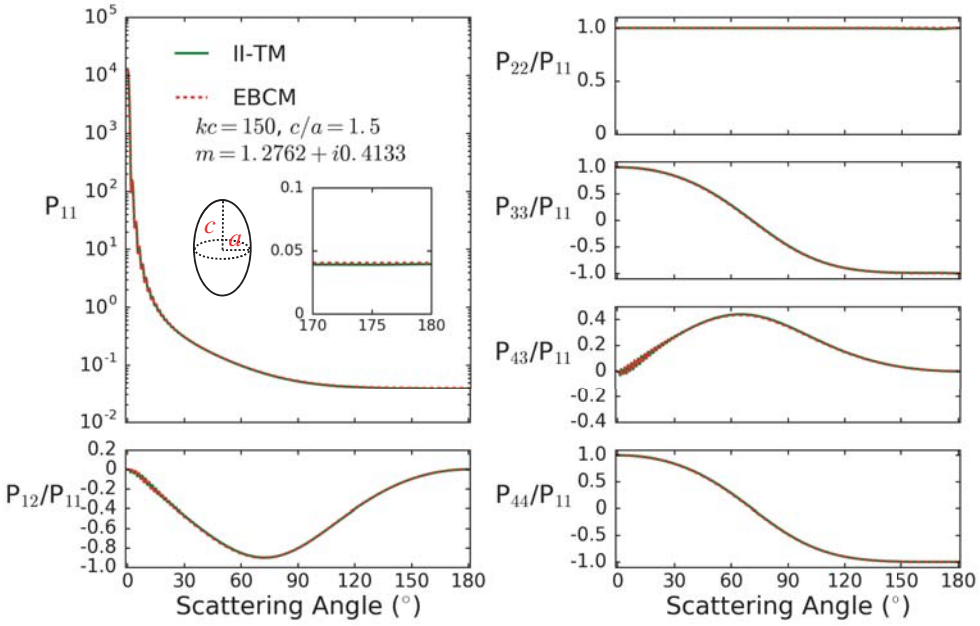

Figure 8. Comparison of the phase matrix elements computed by EBCM and II-TM. The particle is a prolate spheroid with aspect ratio (c/a) 1.5. The major axis size parameter is 150. The refractive index is $1.2762 + i0.4133$, which is the ice refractive index at wavelength 12 µm. The inset plot shows the P_{11} element for scattering angles 170°–180°.

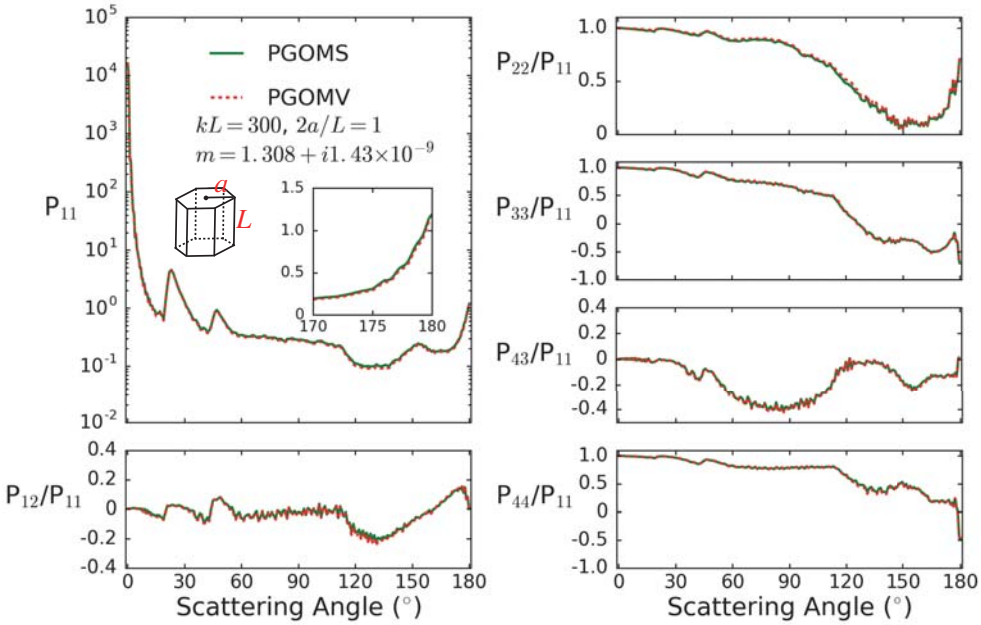

Figure 9. Comparison of the phase matrix elements computed by PGOMS and PGOMV. The particle is a hexagonal column with aspect ratio 1. The size parameter is 300. The refractive index is $1.308 + i1.43 \times 10^{-9}$, the ice refractive index at wavelength 0.65 µm. The inset plot shows the P_{11} element for scattering angles 170°–180°.

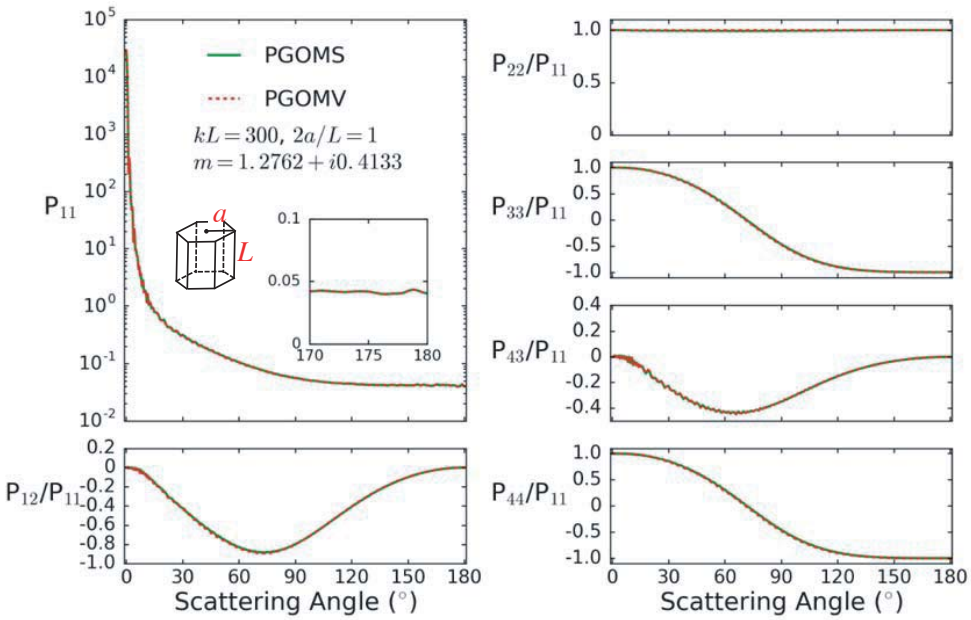

Figure 10. Comparison of the phase matrix elements computed by PGOMS and PGOMV. The particle is a hexagonal column with aspect ratio 1. The size parameter is 300. The refractive index is $1.2762 + i0.4133$, the ice refractive index at 12 μm wavelength. The inset plot shows the P_{11} element for scattering angles 170°–180°.

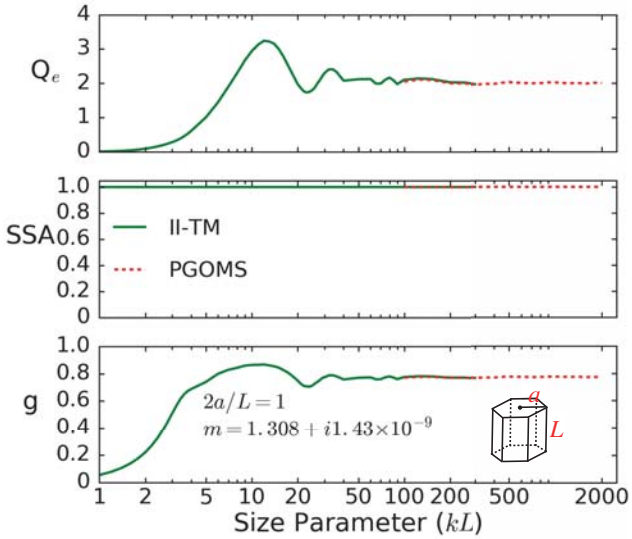

Figure 11. Extinction efficiency (Q_e), single-scattering albedo (SSA), and asymmetry factor (g) computed by II-TM and PGOMS. The particle is a hexagonal column with aspect ratio 1. The refractive index is $1.308 + i1.43 \times 10^{-9}$, which is the ice refractive index at 0.65 μm wavelength.

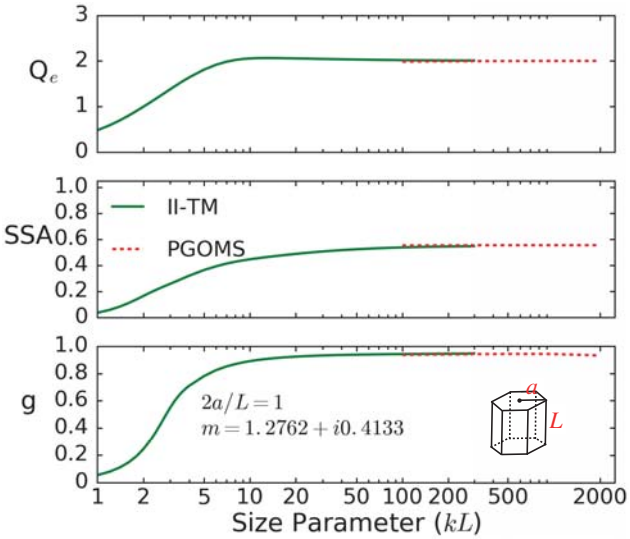

Figure 12. Extinction efficiency (Q_e), single-scattering albedo (SSA), and asymmetry factor (g) computed by II-TM and PGOMS. The particle is a hexagonal column with aspect ratio 1. The refractive index is $1.2762 + i0.4133$, which is the ice refractive index at 12 μm wavelength.

Figures 11 and 12 show the Q_e, SSA, and g for various size parameters computed by II-TM and PGOMS. II-TM is used for size parameter up to $kL = 300$ and PGOMS is used for size parameters larger than 100. In the overlap range and especially at a connection point of $kL = 300$, the two methods converge. The differences are insignificant in Figs. 11 and 12. The oscillation features of Q_e

and g at a visible wavelength (Fig. 11) are clearly captured by both methods. Q_e converges to 2 at both wavelengths with increasing size parameter (Figs. 11 and 12).

Figures 13 and 14 show the scattering phase matrices of the hexagonal column computed by II-TM and PGOMS. The particle size parameters are kL = 100, 200, and 300. As the size parameter increases, the PGOMS results tend to become closer to the II-TM results. This implies that the geometric optics approximation is better for larger size parameters. In Fig. 13, the particle is nearly nonabsorbing. PGOMS accurately captures the oscillation features for size parameters larger than $kL = 200$. Specifically, the P_{11} and P_{12}/P_{11} elements computed by PGOMS are essentially identical to the II-TM results. All the nonzero elements in backscattering directions (close to 180°) computed by PGOMS are consistent with the II-TM results. Accurate simulation of P_{11} and P_{12} elements is critical

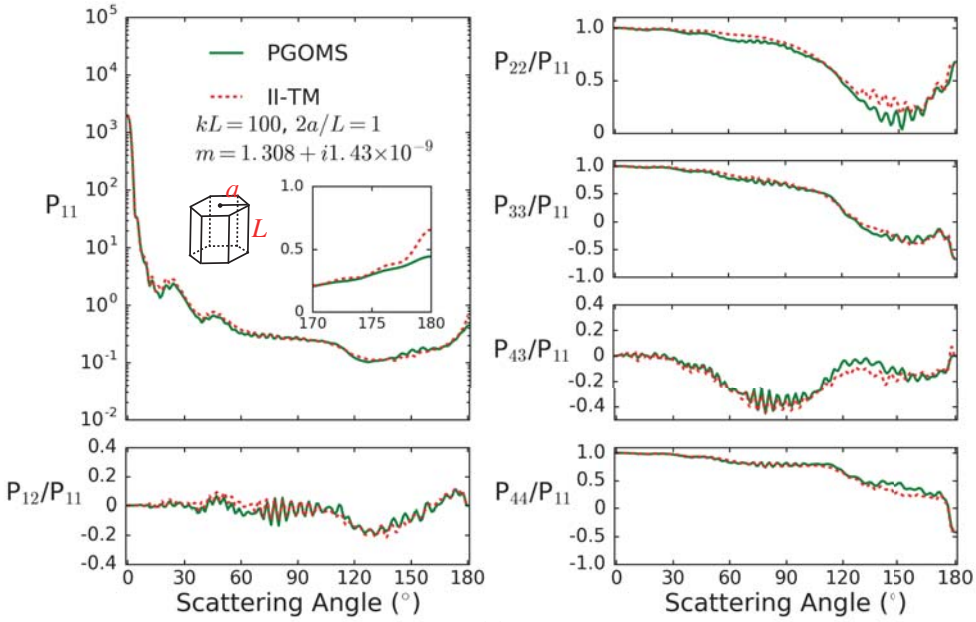

(a)

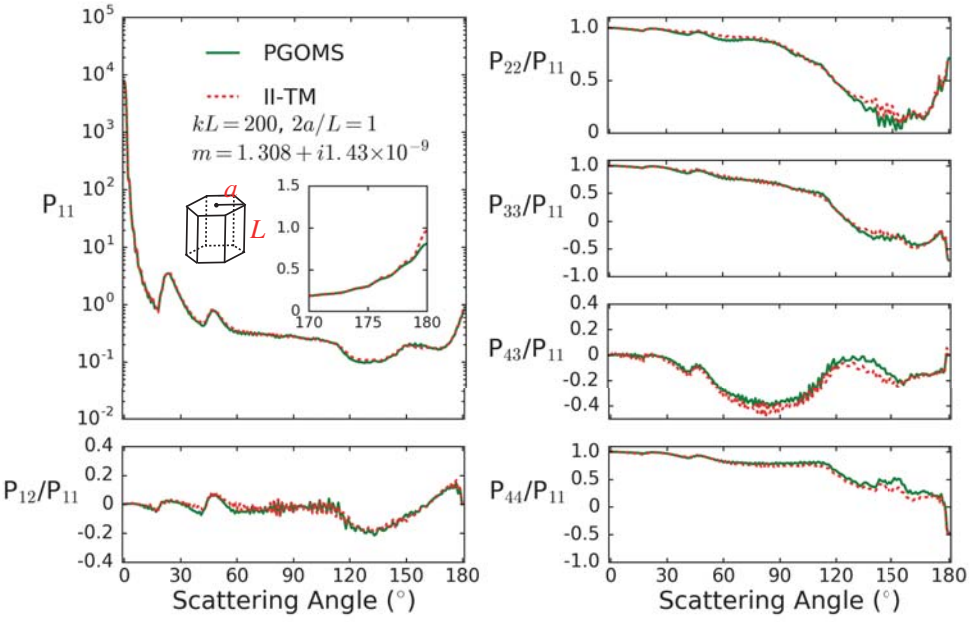

(b)

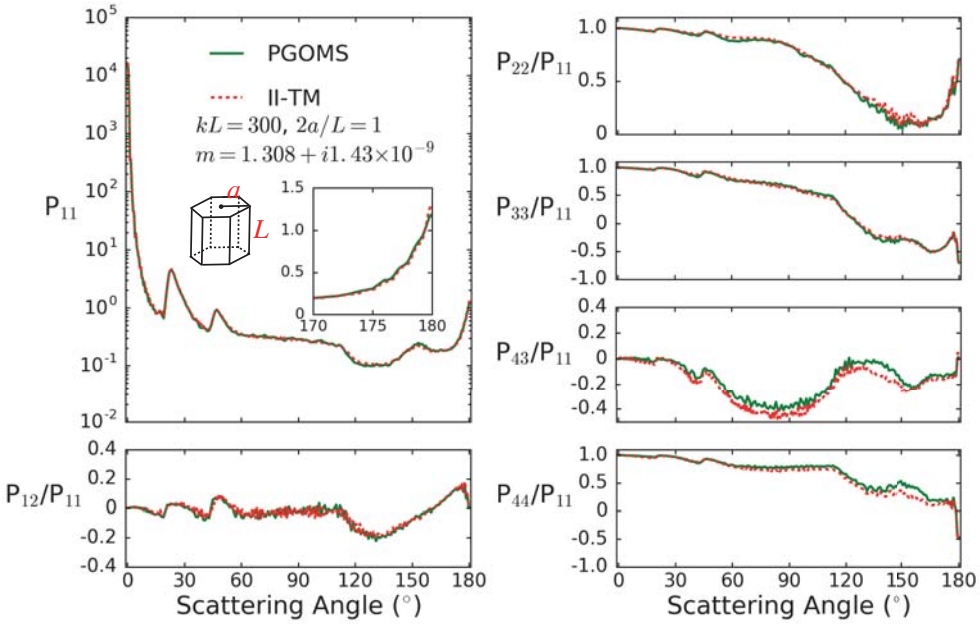

(c)

Figure 13. Comparison of the phase matrix elements computed by PGOMS and II-TM. The particle is a hexagonal column with aspect ratio 1. The refractive index is $1.308 + i1.43 \times 10^{-9}$, which is the ice refractive index at 0.65 μm wavelength. The inset plots show the P_{11} element for scattering angles 170°–180°. (a) Size parameter $kL = 100$; (b) size parameter $kL = 200$; (c) size parameter $kL = 300$.

to remote sensing using a polarimeter, and accurate backscattering calculations will benefit lidar remote sensing. In Fig. 14 the particle is strongly absorptive. The phase matrix is featureless compared to nonabsorbing particles. The consistency of II-TM and PGOMS is also shown in Fig. 14.

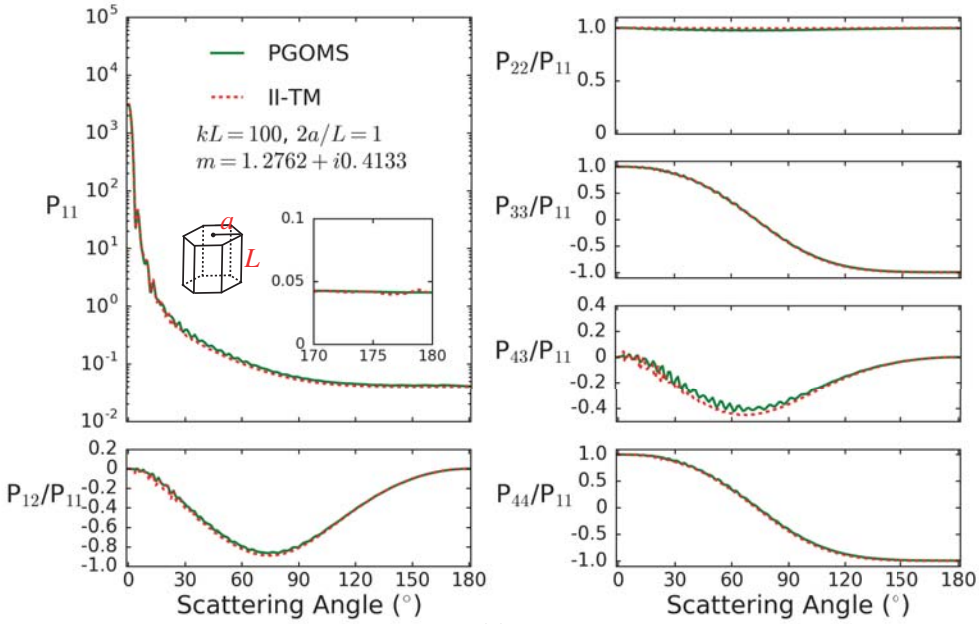

(a)

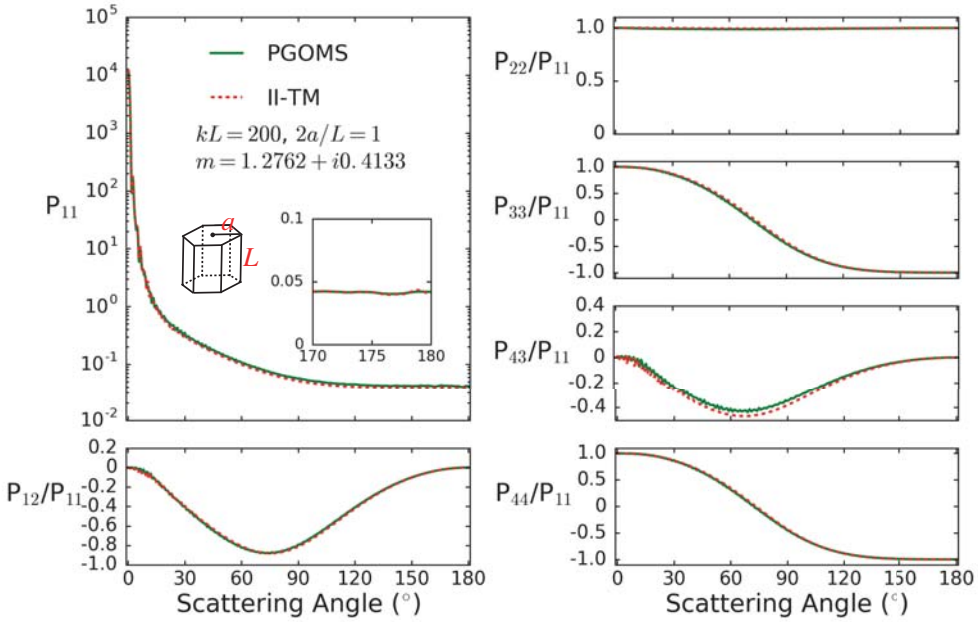

(b)

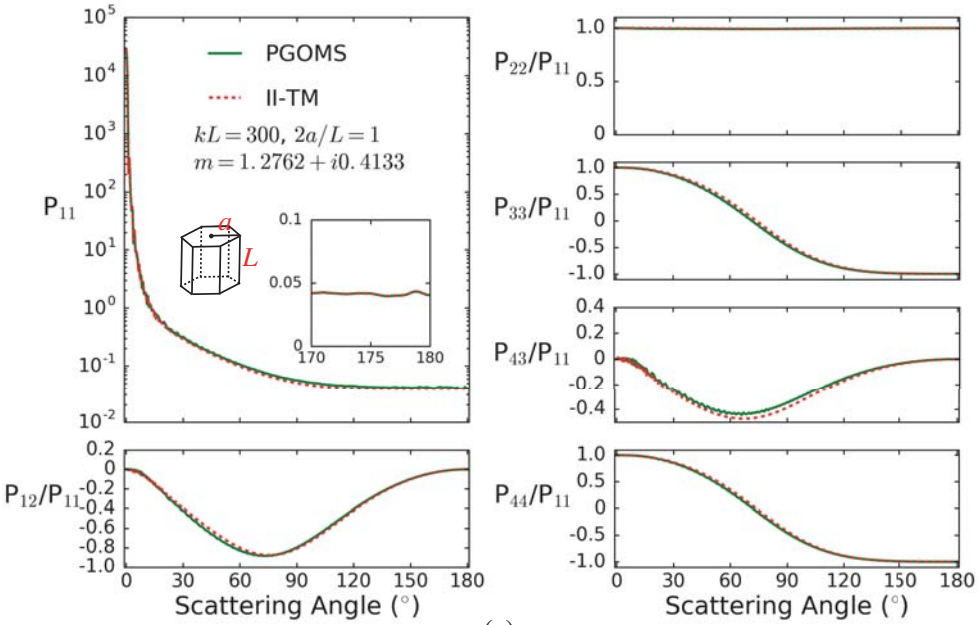

(c)

Figure 14. Comparison of the phase matrix elements computed by PGOMS and II-TM. The particle is a hexagonal column with aspect ratio 1. The refractive index is $1.2762 + i0.4133$ the ice refractive index at 12 µm wavelength. The inset plots show the P_{11} element for scattering angles 170°–180°. (a) Size parameter $kL = 100$; (b) size parameter $kL = 200$; (c) size parameter $kL = 300$.

4.3. IGOM and II-TM Comparison

This subsection compares II-TM and the improved geometric optics method (IGOM), which is a simplified form of PGOMS, developed by Yang and Liou [47]. The IGOM version used here is based on the surface-integral equation, but the wave interference is not fully considered. Instead, the ray-spreading effect is taken into account by the intensity mapping technique detailed in [47]. Compared

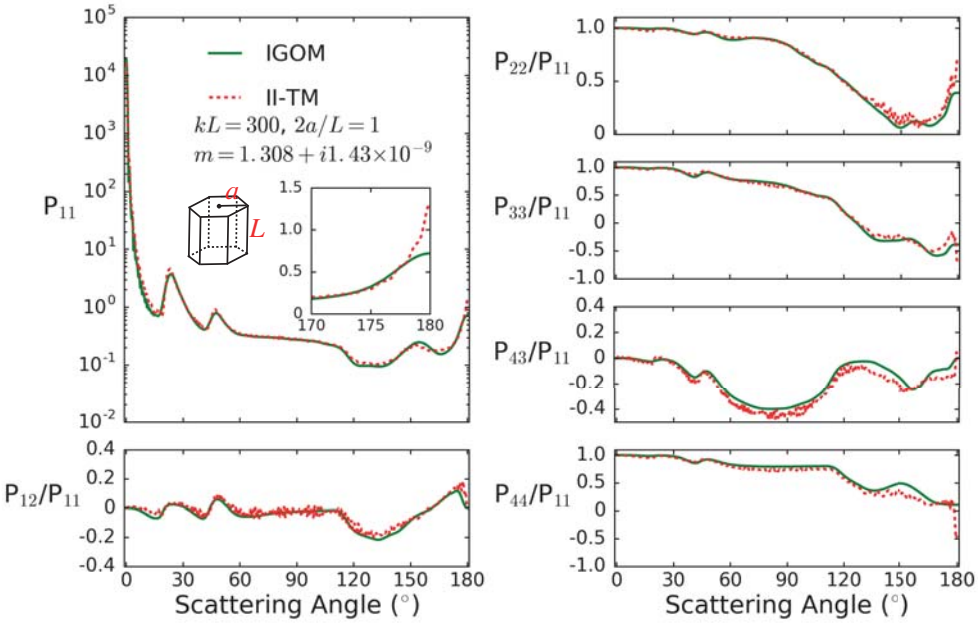

Figure 15. Comparison of the phase matrix elements computed by IGOM and II-TM. The particle is a hexagonal column with aspect ratio 1. The size parameter is 300. The refractive index is $1.308 + i1.43 \times 10^{-9}$, the ice refractive index at 0.65 μm wavelength. The inset plot shows the P_{11} element for scattering angles 170°–180°.

with PGOM, IGOM contains more approximations to reduce its demand on computational resources. Figs. 15 and 16 show the scattering phase matrices of the hexagonal column computed by IGOM and II-TM. In Fig. 15, the nearly nonabsorbing case, IGOM captures overall features of the phase matrix such as halo peaks. However, IGOM smooths out the oscillations that are clearly shown in the II-TM results. In addition, substantial errors of the IGOM solution are found in the phase function in backscattering directions (178°–180°). In Fig. 16, the strongly absorbing case, IGOM is as good as PGOM. For a strongly absorbing particle, most scattering information comes from diffraction and external reflection processes that are accurately computed in both PGOM and IGOM. Therefore, PGOM is a better choice to accurately compute the single-scattering properties of large particles.

4.4. Application to Particle Aggregates

The previous subsections present the comparisons among II-TM, PGOM, and IGOM for convex particle scattering calculations. Ishimoto et al. [79] use FDTD and geometric optics methods to model the optical properties of ice aggregates. Here we demonstrate the applications of II-TM, PGOM, and IGOM to the computation of the single-scattering properties of aggregates.

As mentioned in Section 3, for a concave particle, mapping the near field to the far field should be implemented on a closed and connected surface enclosing the particle. In this study, we use a rectangular box to enclose the particle, and map the near field on the box. To validate the approach, we first try a convex particle (e.g., hexagonal column). Fig. 17 shows the comparison of phase matrix computations by PGOMS with two different mapping schemes. One scheme maps the near field on the particle surface, the same mapping as in Subsection 4.2 (Figs. 9 and 10). Another scheme maps the near field on the enclosing box. The result suggests that the box surface mapping scheme is consistent with the particle surface mapping scheme. Only slight differences can be seen in some small features in Fig. 17. In later contexts, when PGOMS is applied to a concave particle, the box surface mapping scheme is used.

Figure 18 shows the phase matrix of an aggregate of 4 hexagonal columns computed by II-TM and PGOMS. In this aggregate, all the 4 elements have aspect ratio 1. The size parameter is 180

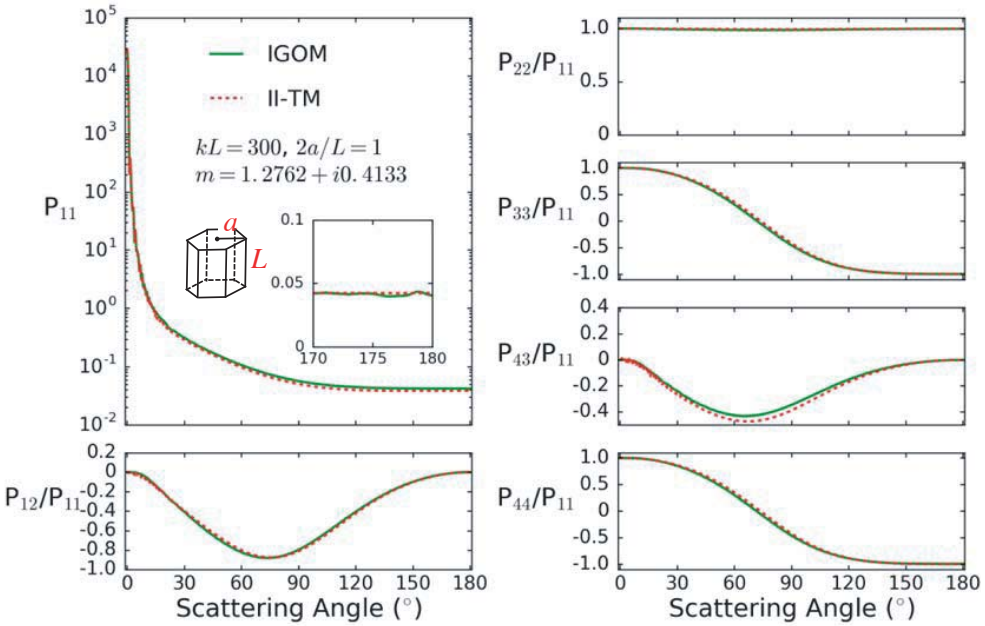

Figure 16. Comparison of the phase matrix elements computed by IGOM and II-TM. The particle is a hexagonal column with aspect ratio 1. The size parameter is 300. The refractive index is $1.2762+i0.4133$, which is the ice refractive index at 12 μm wavelength. The inset plot shows the P_{11} element for scattering angles 170°–180°.

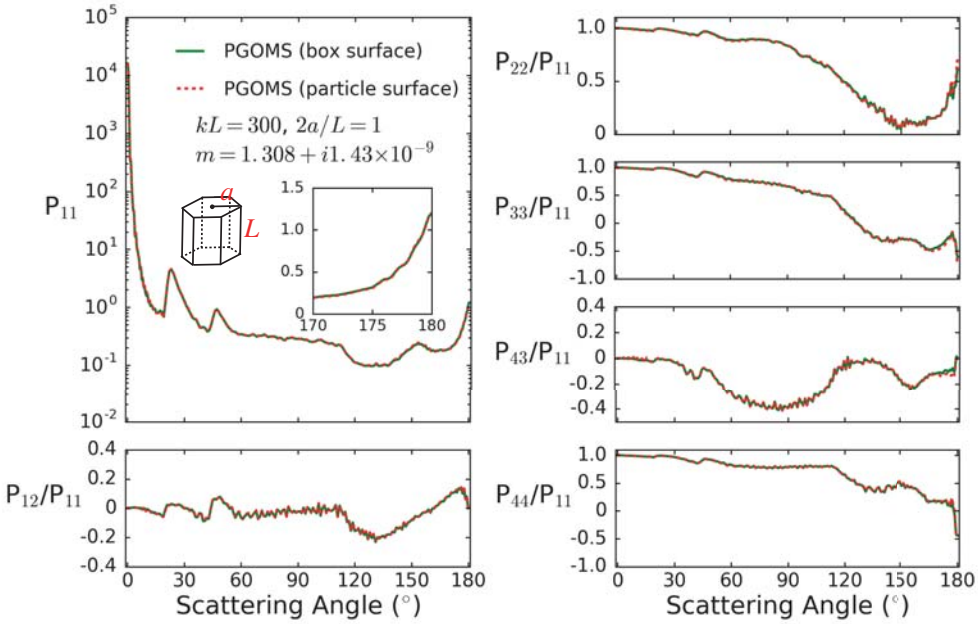

Figure 17. Comparison of the phase matrix elements computed by two setups of PGOMS, mapping the near field on a box surface enclosing the particle (PGOMS (box surface)), or mapping the near field on the particle surface (PGOMS (particle surface)). The particle is a hexagonal column with aspect ratio 1. The size parameter is 300. The refractive index is $1.308+i1.43\times10^{-9}$, which is the ice refractive index at wavelength 0.65 μm. The inset plot shows the P_{11} element for scattering angles 170°–180°.

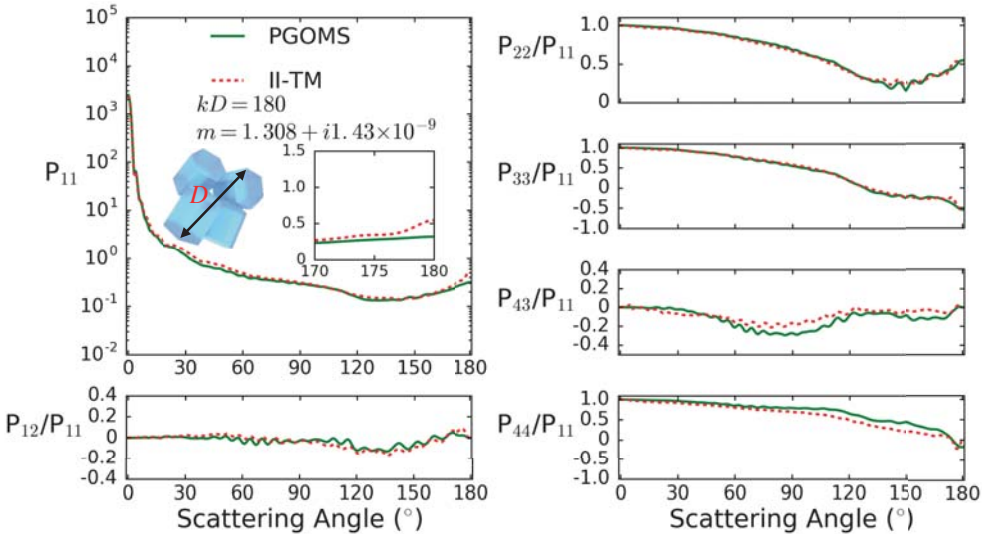

Figure 18. Comparison of the phase matrix elements computed by PGOMS and II-TM. The particle is a 4-hexagonal column aggregate. All the aggregate elements have aspect ratio 1. The refractive index is $1.308 + i1.43 \times 10^{-9}$, which is the ice refractive index at 0.65 μm wavelength. The inset plot shows the P_{11} element for scattering angles 170°–180°. D is the maximum dimension of the particle. The size parameter (kD) is 180.

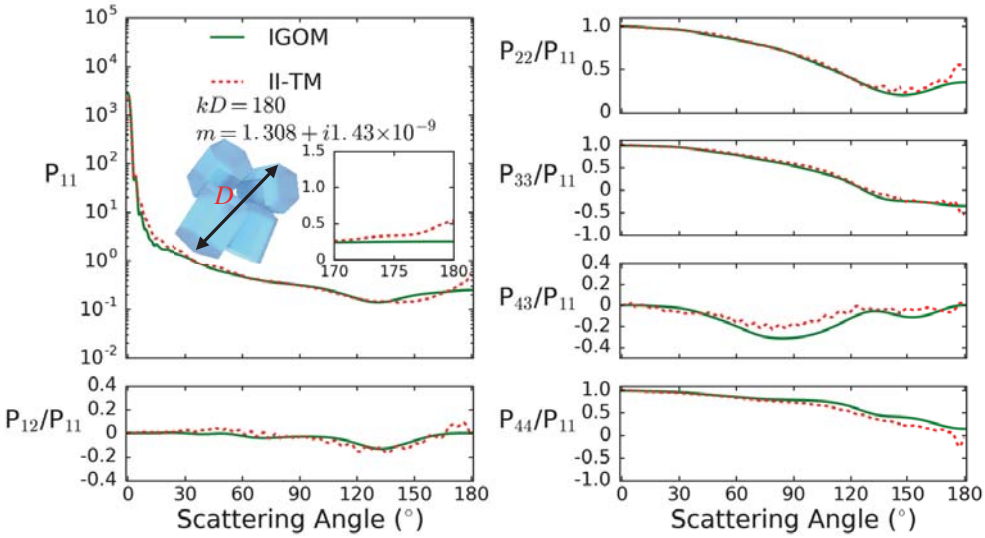

Figure 19. Comparison of the phase matrix elements computed by IGOM and II-TM. The particle is a 4-hexagonal column aggregate. All the aggregate elements have aspect ratios 1. The refractive index is $1.308 + i1.43 \times 10^{-9}$, which is the ice refractive index at 0.65 μm wavelength. The inset plot shows the P_{11} element for scattering angles 170°–180°. D is the maximum dimension of the particle. The size parameter (kD) is 180.

and is defined by its maximum dimension. In general, the II-TM and PGOMS results are consistent. The PGOMS errors are attributed to the inherent inaccuracy associated with the geometric optics approximation. Although the maximum dimension size parameter is 180, some of the morphologic features of the particle correspond to size parameters much smaller than 180. The geometric optics approximation is not sufficiently accurate for characterizing these small features.

Figure 19 shows the phase matrix of the same 4-hexagonal column aggregate computed by II-TM

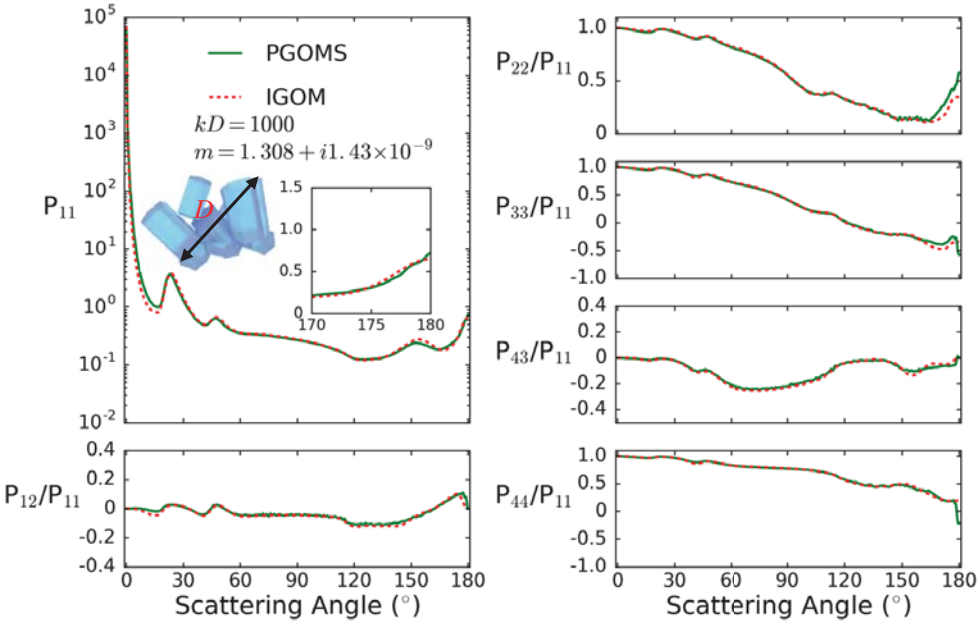

Figure 20. Comparison of the phase matrix elements computed by IGOM and II-TM. The particle is an 8-hexagonal column aggregate. The refractive index is $1.308 + i1.43 \times 10^{-9}$, the ice refractive index at 0.65 µm wavelength. The inset plot shows the P_{11} element for scattering angles 170°–180°. D is the maximum dimension of the particle. The size parameter (kD) is 1000.

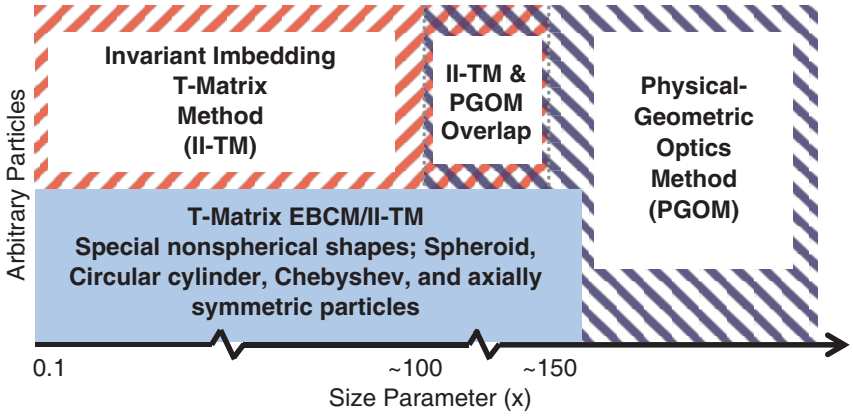

Figure 21. Schematic illustration of the overlapped applicable size-parameter regime of II-TM and PGOM.

and IGOM. Obviously, IGOM has worse performance than PGOMS, particularly in the backscattering directions. Fig. 20 shows the phase matrix of an aggregate of 8 hexagonal columns as defined in [80]. The size parameter is 1000, where the geometric optics approximation is highly accurate. The PGOMS and IGOM results are overall consistent except for the backscattering directions. This suggests that the two different geometric optics methods converge at large size parameters.

From the above numerical results, we see good agreement between II-TM and PGOM for large size parameters. The convergence of the exact method and approximate method is obtained. The single-scattering properties computed at the upper limit of the exact method and the lower limit of the approximate method are almost overlapping. Connecting the two methods at a size parameter of approximately 150, we are able to accurately model particle scattering properties ranging from the Rayleigh to the geometric optics regimes as shown in Fig. 21 (size parameters 0.1 to 2000 in this study).

5. APPLICATION TO REMOTE SENSING

To illustrate the application of a combination of II-TM and PGOM for practical light-scattering calculations, here we consider the single-scattering of airborne dust aerosol particles that are exclusively nonspherical. It is not realistically feasible to account for the extremely complex morphologies of natural dust particles in light scattering computations used by remote sensing implementations and radiative transfer simulations. Following Bi et al. [81], we consider the single-scattering properties of an ensemble of randomly distorted hexahedra as the surrogates for the realistic dust particles. In simple terms, a hexahedron is distorted by tilting each face by a random angle, so the distorted hexahedron still has six flat faces, but they are not rectangular and opposite faces are not parallel. As an example, consider the top facet of a regular hexahedron shown in Fig. 22 as an example. Following Yang and Liou [82], the facet is randomly tilted around its center point with the following two angles:

$$\varphi_{\text{face}} = 2\pi\xi_1, \tag{45a}$$

$$\theta_{\text{face}} = \cos^{-1}\left[1/\left(1-\sigma^2\ln\xi_2\right)\right], \tag{45b}$$

where ξ_1 and ξ_2 are two random numbers with a uniform probability distribution in (0, 1), and φ rotation is carried out first. σ is a parameter indicating the degree of random tilting. As σ becomes larger, the more distorted the particle is in comparison with a regular hexahedron. The above equations imply that the slopes of the tilted facet along two orthogonal directions (the relative coordinates are denoted as η and ζ) with respect to the un-tilted facet are given by Yang and Liou [82],

$$P(h_\eta, h_\varsigma) = \frac{1}{\pi\sigma^2}\exp\left[\left(-\left(h_\eta^2+h_\varsigma^2\right)/\sigma^2\right]\right., \tag{46}$$

where h indicates the deviation of a point on the tilted facet from the un-tilted counterpart. The slopes are given by

$$h_\eta = \frac{\partial h}{\partial \eta}, \tag{47a}$$

$$h_\varsigma = \frac{\partial h}{\partial \varsigma}, \tag{47b}$$

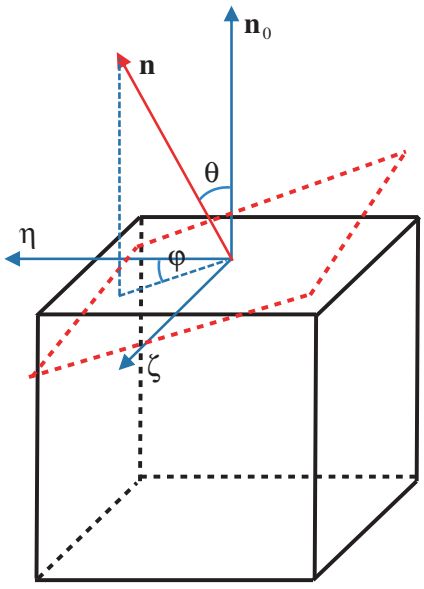

Figure 22. The geometry of facet tilting on a hexahedron. η and ζ are relative coordinates. θ and φ are tilting angles and φ rotation is carried out first. $\mathbf{n}_0$ is the normal vector of the facet before tilting, and $\mathbf{n}$ is the normal vector of the tilted facet.

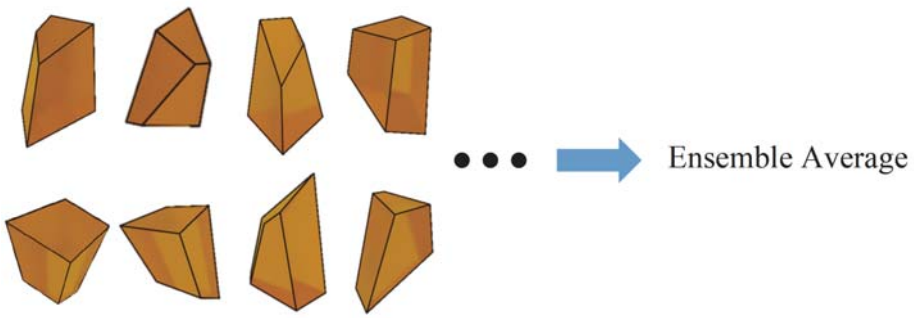

Figure 23. 8 examples of the randomly distorted hexahedral particles.

Figure 23 shows 8 examples of the randomly distorted hexahedral particles. The ensemble-averaged single-scattering properties (the phase matrix, extinction efficiency, and single-scattering albedo) are given by

$$P = \frac{\sum_{i=1}^{N} P_i Q_{sca,i} A_{proj,i}}{\sum_{i=1}^{N} Q_{sca,i} A_{proj,i}}, \tag{48a}$$

$$Q_{ext} = \frac{\sum_{i=1}^{N} Q_{ext,i} A_{proj,i}}{\sum_{i=1}^{N} A_{proj,i}}, \tag{48b}$$

$$SSA = \frac{\sum_{i=1}^{N} Q_{sca,i} A_{proj,i}}{\sum_{i=1}^{N} Q_{ext,i} A_{proj,i}}, \tag{48c}$$

where N is the total number of the particles considered in the ensemble average. Q_{ext} and Q_{sca} are the extinction and scattering efficiencies, respectively, and A_{proj} is the projected area.

Figure 24 shows the theoretical phase matrix simulations based on three models, an ensemble of hexahedra, a mixture of oblate and prolate spheroids, and spheres in comparison with measurements [83] for small olivine particles at 632.8 nm. A lognormal size distribution is assumed to compute the size-averaged phase matrices. The lognormal distribution probability density function (PDF) is defined as

$$p(r) = \frac{1}{\sqrt{2\pi} r\sigma} \exp\left[-\frac{\ln r - \ln \mu}{2\sigma^2}\right], \tag{49}$$

where σ and μ are two parameters. In the calculation, σ is 2.0 and μ is 1.5.

Numerous measurements (e.g., [84–87]) found that aspect ratios of dust particles range between 1.0 and 2.3 with mode or mean values 1.4, 1.7, 1.9, 2 and 2.2. Following Mishchenko et al. [88], in this study we assume the aspect ratio of a hexahedron to be 1.7. In addition, we also consider a mixture of prolate ($c/a = 1.7$) and oblate ($a/c = 1.7$) spheroidal geometries. We tried various mixing ratios of prolate and oblate spheroids, and found a mixture of 99.8% prolate spheroids and 0.2% oblate spheroids to have minimum least-square error compared with the measurements [83]. It can be seen from Fig. 24 that the phase matrix based on the randomly distorted hexahedron model agrees with the measurements. It is also obvious from Fig. 24 that the sphere model is not applicable to the simulation of the optical

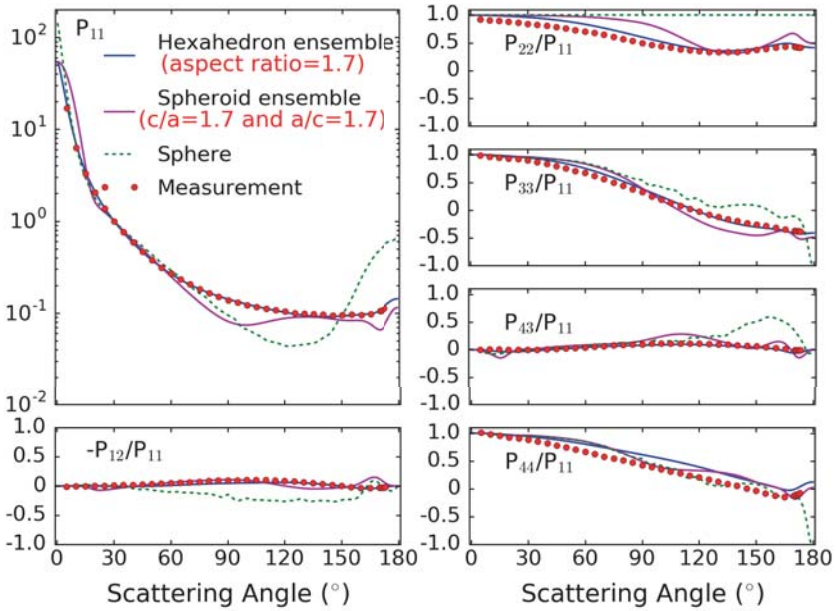

Figure 24. Comparison of phase matrices of the hexahedron ensemble model, the spheroid ensemble model, and the sphere model with lab measurement. The measured phase matrix data is for small olivine particles from the Amsterdam light scattering database [83] at 0.633 μm.

properties of dust aerosols. Although the results based on the spheroid model substantially deviate from the measurements, it should be pointed out that spheroids can be used to approximate dust particles in light-scattering calculations if an appropriate aspect ratio distribution is assumed, as demonstrated by Mishchenko et al. [89] and Dubovik et al. [90].

We then utilize the hexahedron ensemble and sphere models to represent dust aerosols in a radiative transfer simulation that includes the full polarization state. We simulate the normalized modified polarized reflectivity (L_{nmp}) from dust aerosols observed by the POLarization and Directionality of the Earth's Reflectances (POLDER) instrument [91] onboard the Polarization & Anisotropy of Reflectances for Atmospheric Sciences coupled with Observations from a Lidar (PARASOL) satellite. L_{nmp} is defined as

$$L_{nmp} = \mathrm{sgn}\frac{\pi\left(\cos\theta + \cos\theta_0\right)\sqrt{Q^2+U^2}}{F_0\cos\theta_0}, \tag{50}$$

where θ_0 is the solar zenith angle; θ is the viewing zenith angle; F_s is the solar irradiance; Q and U are the Stokes components representing linear polarization; and sgn is either 1 or -1 [92]. The radiative transfer model developed by Huang et al. [93] is used in this study, which utilizes the adding-doubling technique to compute the full Stokes vector. The lowest boundary in the simulation is assumed to be an ocean surface with wind speed 10 m/s. The roughness of the ocean surface is modeled according to Cox and Munk [94].

A comparison between the simulations and selected POLDER observations is shown in Fig. 25. In the simulation, the dust layer has aerosol optical thickness (τ) 2.0, and effective radius (r_{eff}) 0.9 μm. We select a dust storm event on 27 June 2007 over the Red Sea observed by POLDER on the PARASOL satellite. The location is shown in the upper panel of Fig. 25. The lower panel in Fig. 25 shows that the radiative transfer simulations based on the hexahedron ensemble model are much closer to the observations than the sphere model counterparts. This suggests that the nonspherical hexahedron ensemble model is more realistic and should perform better in an aerosol property retrieval algorithm.

We construct a retrieval algorithm based on the Levenberg-Marquardt method [90] to infer τ and r_{eff} from POLDER observations. The algorithm can be expressed by an iterative equation,

$$\mathbf{x}^{n+1} = \mathbf{x}^n - t\left(\mathbf{J}^T\mathbf{C}^{-1}\mathbf{J} + \gamma\mathbf{D}\right)^{-1}\mathbf{J}^T\mathbf{C}^{-1}\left(\mathbf{f}(\mathbf{x}^n) - \mathbf{f}_m\right), \tag{51}$$

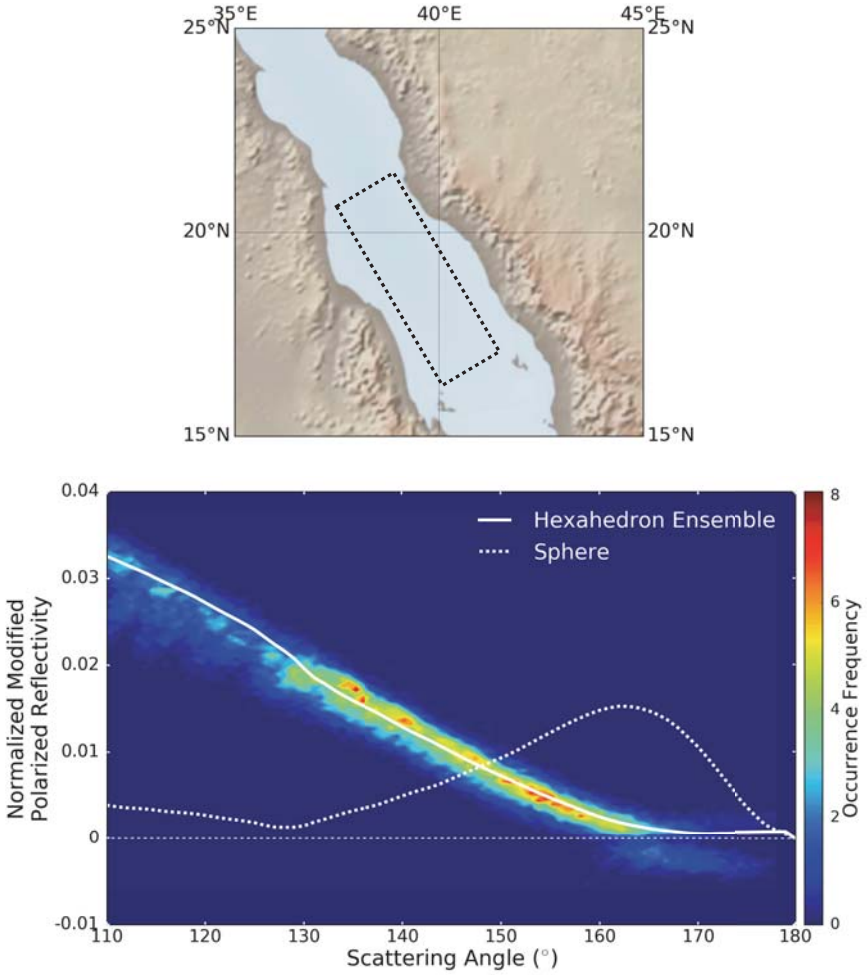

Figure 25. Observed and simulated normalized modified polarized reflectivity (L_{nmp}) from dust aerosols over the Red Sea. The upper panel is the location of the dust aerosol observation. The data from the dashed rectangle area in the upper panel is shown in the lower panel. The lower panel shows the observed and simulated L_{nmp} at wavelength 0.865 µm. The color contour indicates number of pixel-level observations. The white solid line is the simulation assuming the hexahedron ensemble model for dust aerosols. The white dashed line is the simulation assuming spheres as the dust aerosol.

in which $\mathbf{x}$ is the variable vector that has two elements, τ and r_{eff}; $\mathbf{J}$ is the Jacobian matrix; $\mathbf{f}(\mathbf{x})$ is the simulated multi-angle reflectivity and polarized reflectivity; $\mathbf{f}_m$ is the measured multi-angle reflectivity and polarized reflectivity; and $\mathbf{D}$ is the unity matrix. Here t and γ are two constants determined empirically, and n is the order of iteration. A look-up table (LUT) is computed by the simulator mentioned above. It contains multi-angle reflectivity and polarized reflectivity for tabulated observation geometries, τ and r_{eff}. $\mathbf{f}(\mathbf{x})$ and $\mathbf{J}$ are obtained by interpolating the LUT. $\mathbf{x}^1$ is the initial vector and is assigned a random value. By iteratively computing Eq. (51), $\mathbf{x}^n$ converges to a value where the sum of squared errors between simulated and measured quantities is the smallest. The τ and r_{eff} in $\mathbf{x}^n$ are the retrieved results.

Here we illustrate the retrieval results over the east Atlantic Ocean during a Saharan dust storm. The retrieved result shown in Fig. 26 is for the POLDER observation on 21 September 2009. In the retrieval, the dust aerosols are assumed to be African dust with refractive index data from [95]. From Figs. 26(c)–(d), the retrieved τ values are mainly in the range $0.4 \sim 1.2$, and r_{eff} around 0.8 µm. The spatial distributions of the retrieved τ and r_{eff} are shown in Figs. 26(a)–(b). The area closer to the coast tends to have larger τ and r_{eff}, which may reveal the deposition process when the dust aerosol

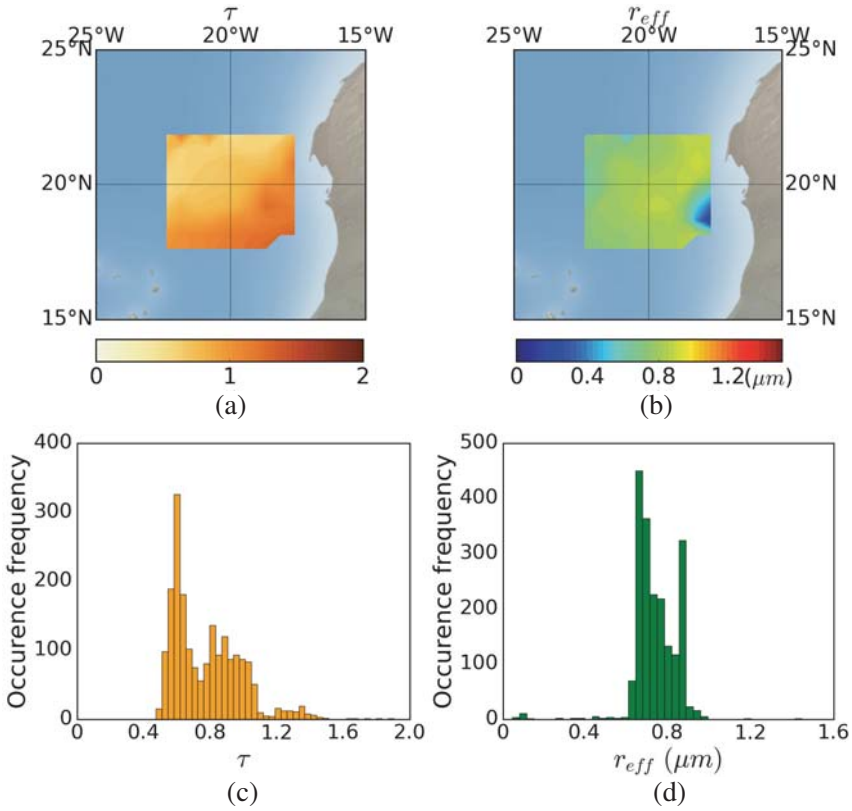

Figure 26. Dust aerosol optical thickness (τ) and effective radius (r_{eff}) retrieval results. (a) Retrieved τ by assuming African dust aerosol model; (b) retrieved r_{eff} by assuming African dust aerosol model; (c) retrieved τ value distribution; (d) retrieved r_{eff} value distribution.

transports away from the coast, as larger particles fall out more quickly.

To show the impact of using an inappropriate dust aerosol model on retrieval results, we also implement the retrieval algorithm by assuming Asian dust for the index of refraction of dust compiled in the same dataset [95]. The differences between the two retrieval results are shown in Fig. 27. The two different dust refractive indices as functions of particle size are shown in Fig. 28. As an example, the phase matrix elements P_{11} and P_{12}/P_{11} of the two dust models are shown in Fig. 29. The reflectivity and polarized reflectivity are mainly determined by P_{11} and P_{12}/P_{11}, respectively. Different refractive indices give different single-scattering property results, as shown in Fig. 29. Thus, the LUTs for the

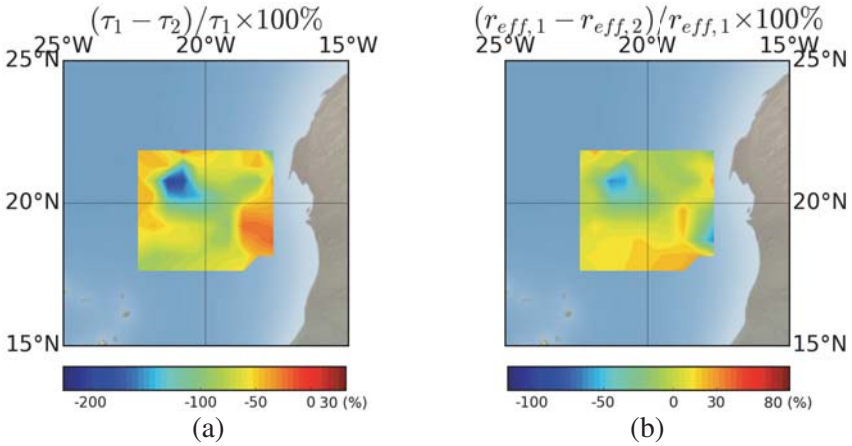

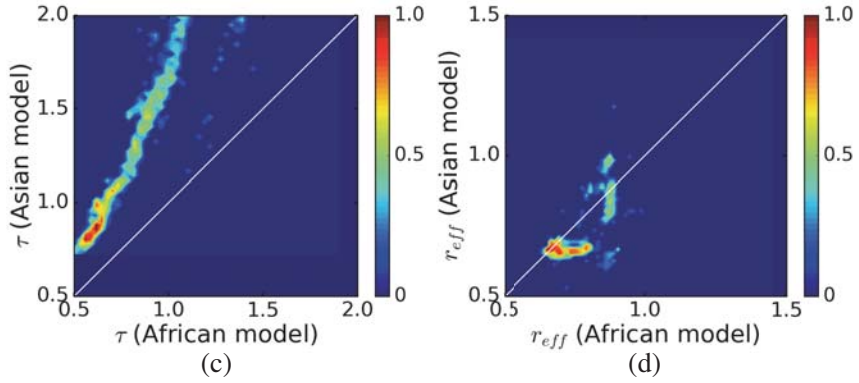

Figure 27. (a) Percentage difference between τretrieved by assuming African (τ_1) and Asian (τ_2) dust aerosol models; (b) percentage difference between r_{eff} retrieved by assuming African ($r_{eff,1}$) and Asian ($r_{eff,2}$) dust aerosol models; (c) one-to-one comparison between retrieved τ by assuming the two dust models; (d) one-to-one comparison between r_{eff} retrieved by assuming the two dust models. In (c) and (d), the white straight lines are one-to-one ratio lines.

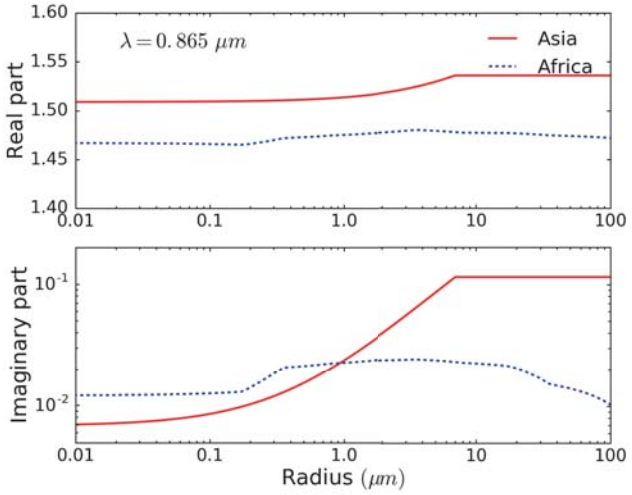

Figure 28. Observed dust refractive indices at wavelength 0.865 µm in Asia and Africa as functions of particle size based on the compilation by Stegmann and Yang [95].

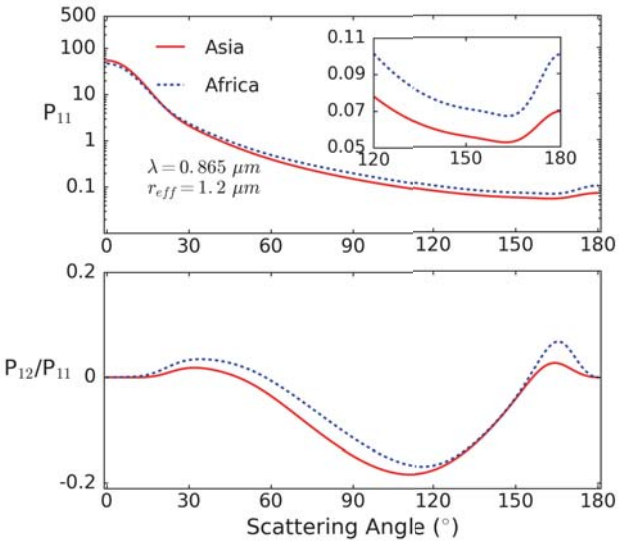

Figure 29. P_{11} and P_{12} phase matrix elements of Asian and African dust models with effective radius 1.2 µm at wavelength 0.865 µm.

retrieval implementation are different, which affects the retrieval results. As shown in Fig. 27, the retrieval results, especially τ, are quite sensitive to the index of refraction assumed in the forward light-scattering computation. The retrieved τ values by assuming Asian dust are almost twice the counterparts by assuming African dust.

6. SUMMARY

The convergence of II-TM and PGOM in computing nonspherical dielectric particle scattering properties is illustrated following a brief introduction of the two methods. II-TM is used for particle size parameters up to 150. Taking hexagonal column ice crystals as an example, the present numerical results show that up to around size parameter 200, II-TM and PGOM agree well. We simulate the particle extinction

efficiency, single-scattering albedo, asymmetry factor, and phase matrix at two wavelengths where ice is nearly nonabsorbing (0.65 μm) and strongly absorbing (12 μm). All results show that II-TM and PGOM converge at a size parameter ~ 150, where both of the methods are accurate. Because II-TM compares well with the conventional EBCM for application to spheroidal particles, II-TM is considered accurate enough as a benchmark to test approximate methods. Although both PGOM and IGOM are accurate for large strongly absorbing particles, for less absorbing particles, only PGOM is able to simulate nearly all phase matrix features and can accurately compute backscattering. A synergetic combination of II-TM and PGOM can therefore be seamlessly applied to the entire size parameter domain extending from the Rayleigh regime to the geometric optics regime. Furthermore, we illustrate the applicability of the present light-scattering capability in simulating the optical properties of dust aerosol in conjunction with remote sensing of dust aerosol radiative and microphysical properties, namely optical thickness and effective particle size.

ACKNOWLEDGMENT

The authors acknowledge Dr. Bingqing Sun's contributions to some theoretical derivations and a portion of the invariant imbedding T-matrix simulations involved in this paper, while he was working at Texas A&M University. This research was supported by the National Science Foundation, grant number AGS-1826936, and partly by the Texas A&M David Bullock Harris Chair in Geosciences endowment funds, grant number 02-512231-00001. Dr. Mishchenko was supported by the NASA Radiation Sciences Program and Remote Sensing Theory Program.

APPENDIX A.

Concave Particle Projected Area Computation

Without loss of generality, we take a hexagonal plate aggregate particle as an example to describe the method to compute a concave particle projected area. The particle is shown in Fig. A1. It is composed of 10 hexagonal plates.

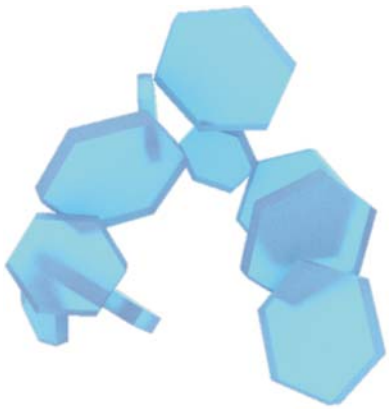

Figure A1. Hexagonal plate aggregate particle.

The method has five steps. First, as shown in Fig. A2(a), the particle is projected on a 2-D plane perpendicular the incident direction, where the projected area will be computed. The particle has 10 convex parts. Second, we use the Convex Hull algorithm [96] to obtain the outline of each convex part, as shown in Fig. A2(b). Third, we merge all the convex parts into one concave polygon, as shown in Fig. A2(c). We modify the Weiler-Atherton polygon clipping algorithm [72] to make it suitable for merging polygons. Fourth, the concave polygon is divided into many triangles, as shown in Fig. A2(d) by using the Ear-cutting algorithm [97]. Finally, we compute the areas of all triangles and sum them up to obtain the projected area of the particle on a plane perpendicular to the specified direction.

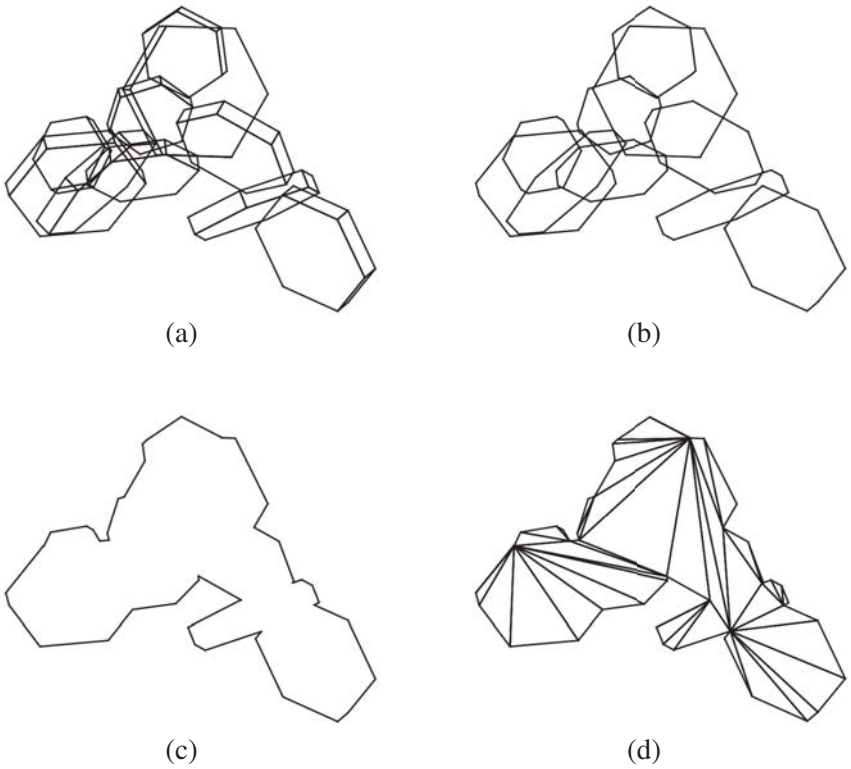

Figure A2. Example to show the steps to compute the projected area of a concave particle.

REFERENCES

1. Mishchenko, M. I., J. W. Hovenier, and L. D. Travis, *Light Scattering by Nonspherical Particles*, Academic Press, 2000.
2. Baran, A. J., "A review of the light scattering properties of cirrus," *J. Quant. Spectrosc. Radiat. Transf.*, Vol. 110, Nos. 14–16, 1239–1260, Sep. 2009.
3. Baran, A. J., "From the single-scattering properties of ice crystals to climate prediction: A way forward," *Atmos. Res.*, Vol. 112, 45–69, Aug. 2012.
4. Baran, A. J., P. Yang, and S. Havemann, "Calculation of the single-scattering properties of randomly oriented hexagonal ice columns: A comparison of the T-matrix and the finite-difference time-domain methods," *Appl. Opt.*, Vol. 40, No. 24, 4376, Aug. 2001.
5. Liou, K. N. and P. Yang, *Light Scattering by Ice Crystals: Fundamentals and Applications*, Cambridge University Press, 2016.
6. Lu, J. Q., P. Yang, and X.-H. Hu, "Simulations of light scattering from a biconcave red blood cell using the finite-difference time-domain method," *J. Biomed. Opt.*, Vol. 10, No. 2, 024022, 2005.
7. Kolesnikova, I. V., S. V. Potapov, M. A. Yurkin, A. G. Hoekstra, V. P. Maltsev, and K. A. Semyanov, "Determination of volume, shape and refractive index of individual blood platelets," *J. Quant. Spectrosc. Radiat. Transf.*, Vol. 102, No. 1, 37–45, Nov. 2006.
8. Bi, L. and P. Yang, "Modeling of light scattering by biconcave and deformed red blood cells with the invariant imbedding T-matrix method," *J. Biomed. Opt.*, Vol. 18, No. 5, 055001, May 2013.
9. Yee, K. S., "Numerical solution of initial boundary value problems involving Maxwell's equations in isotropic media," *IEEE Trans. Antennas Propag.*, Vol. 14, No. 3, 302–307, May 1966.
10. Taflove, A. and S. C. Hagness, *Computational Electrodynamics: The Finite-Difference Time-Domain Method*, 3rd edition, Artech House, Boston, MA, 2005.

11. Yang, P. and K. N. Liou, "Finite-difference time domain method for light scattering by small ice crystals in three-dimensional space," *J. Opt. Soc. Am. A*, Vol. 13, No. 10, 2072–2085, Oct. 1996.
12. Yang, P., K. N. Liou, M. I. Mishchenko, and B.-C. Gao, "Efficient finite-difference time-domain scheme for light scattering by dielectric particles: Application to aerosols," *Appl. Opt.*, Vol. 39, No. 21, 3727–3737, Jul. 2000.
13. Sun, W., N. G. Loeb, S. Tanev, and G. Videen, "Finite-difference time-domain solution of light scattering by an infinite dielectric column immersed in an absorbing medium," *Appl. Opt.*, Vol. 44, No. 27, 1977–1983, Sep. 2005.
14. Ishimoto, H., "Radar backscattering computations for fractal-shaped snowflakes," *J. Meteorol. Soc. Japan Ser. II*, Vol. 86, No. 3, 459–469, 2008.
15. Liu, Q. H., "The PSTD algorithm: A time-domain method requiring only two cells per wavelength," *Microw. Opt. Technol. Lett.*, Vol. 15, No. 3, 158–165, Jun. 1997.
16. Liu, Q. H., "The pseudospectral time-domain (PSTD) algorithm for acoustic waves in absorptive media," *IEEE Trans. Ultrason. Ferroelectr. Freq. Control*, Vol. 45, No. 4, 1044–1055, Jul. 1998.
17. Purcell, E. M. and C. R. Pennypacker, "Scattering and absorption of light by nonspherical dielectric grains," *Astrophys. J.*, Vol. 186, 705–714, Dec. 1973.
18. Draine, B. T. and P. J. Flatau, "Discrete-dipole approximation for scattering calculations," *J. Opt. Soc. Am. A*, Vol. 11, No. 4, 1491–1499, Apr. 1994.
19. Yurkin, M. A. and A. G. Hoekstra, "The discrete dipole approximation: An overview and recent developments," *J. Quant. Spectrosc. Radiat. Transf.*, Vol. 106, Nos. 1–3, 558–589, Jul. 2007.
20. Yurkin, M. A., V. P. Maltsev, and A. G. Hoekstra, "The discrete dipole approximation for simulation of light scattering by particles much larger than the wavelength," *J. Quant. Spectrosc. Radiat. Transf.*, Vol. 106, Nos. 1–3, 546–557, Jul. 2007.
21. Liu, C., R. Lee Panetta, and P. Yang, "Application of the pseudo-spectral time domain method to compute particle single-scattering properties for size parameters up to 200," *J. Quant. Spectrosc. Radiat. Transf.*, Vol. 113, No. 13, 1728–1740, Sep. 2012.
22. Waterman, P. C., "Matrix formulation of electromagnetic scattering," *Proc. IEEE*, Vol. 53, No. 8, 805–812, 1965.
23. Waterman, P. C., "Symmetry, unitarity, and geometry in electromagnetic scattering," *Phys. Rev. D*, Vol. 3, No. 4, 825–839, Feb. 1971.
24. Mishchenko, M. I., "Light scattering by randomly oriented axially symmetric particles," *J. Opt. Soc. Am. A*, Vol. 8, No. 6, 871–882, Jun. 1991.
25. Barber, P. and C. Yeh, "Scattering of electromagnetic waves by arbitrarily shaped dielectric bodies," *Appl. Opt.*, Vol. 14, No. 12, 2864–2872, Dec. 1975.
26. Mishchenko, M. I. and L. D. Travis, "Light scattering by polydispersions of randomly oriented spheroids with sizes comparable to wavelengths of observation," *Appl. Opt.*, Vol. 33, No. 30, 7206–7225, Oct. 1994.
27. Mishchenko, M. I., L. D. Travis, and D. W. Mackowski, "T-matrix computations of light scattering by nonspherical particles: A review," *J. Quant. Spectrosc. Radiat. Transf.*, Vol. 55, No. 5, 535–575, May 1996.
28. Tsang, L., J. A. Kong, K.-H. Ding, and C. O. Ao, *Scattring of Electromagnetic Waves: Theories and Applications*, Wiley, New York, 2000.
29. Mackowski, D. W. and M. I. Mishchenko, "Calculation of the T matrix and the scattering matrix for ensembles of spheres," *J. Opt. Soc. Am. A*, Vol. 13, No. 11, 2266–2278, Nov. 1996.
30. Mackowski, D. W. and M. I. Mishchenko, "A multiple sphere T-matrix Fortran code for use on parallel computer clusters," *J. Quant. Spectrosc. Radiat. Transf.*, Vol. 112, No. 13, 2182–2192, Sep. 2011.
31. Mackowski, D. W., "A general superposition solution for electromagnetic scattering by multiple spherical domains of optically active media," *J. Quant. Spectrosc. Radiat. Transf.*, Vol. 133, 264–270, Jan. 2014.

32. Johnson, B. R., "Invariant imbedding T matrix approach to electromagnetic scattering," *Appl. Opt.*, Vol. 27, No. 23, 4861–4873, Dec. 1988.
33. Bi, L., P. Yang, G. W. Kattawar, and M. I. Mishchenko, "Efficient implementation of the invariant imbedding T-matrix method and the separation of variables method applied to large nonspherical inhomogeneous particles," *J. Quant. Spectrosc. Radiat. Transf.*, Vol. 116, 169–183, Feb. 2013.
34. Bi, L., P. Yang, G. W. Kattawar, and M. I. Mishchenko, "A numerical combination of extended boundary condition method and invariant imbedding method applied to light scattering by large spheroids and cylinders," *J. Quant. Spectrosc. Radiat. Transf.*, Vol. 123, No. 4, 17–22, Jul. 2013.
35. Bi, L. and P. Yang, "Accurate simulation of the optical properties of atmospheric ice crystals with the invariant imbedding T-matrix method," *J. Quant. Spectrosc. Radiat. Transf.*, Vol. 138, 17–35, May 2014.
36. Doicu, A., T. Wriedt, and Y. A. Eremin, *Light Scattering by Systems of Particles*, Springer, Berlin, 2006.
37. Mishchenko, M. I. and L. D. Travis, "Capabilities and limitations of a current FORTRAN implementation of the T-matrix method for randomly oriented, rotationally symmetric scatterers," *J. Quant. Spectrosc. Radiat. Transf.*, Vol. 60, No. 3, 309–324, Sep. 1998.
38. Mishchenko, M. I. and A. Macke, "How big should hexagonal ice crystals be to produce halos?," *Appl. Opt.*, Vol. 38, No. 9, 1626–1629, Mar. 1999.
39. Van de Hulst, H. C., *Light Scattering by Small Particles*, Wiley, New York, 1957.
40. Wendling, P., R. Wendling, and H. K. Weickmann, "Scattering of solar radiation by hexagonal ice crystals," *Appl. Opt.*, Vol. 18, No. 15, 2663–2671, Aug. 1979.
41. Cai, Q. and K. N. Liou, "Polarized light scattering by hexagonal ice crystals: Theory," *Appl. Opt.*, Vol. 21, No. 19, 3569–3580, Oct. 1982.
42. Takano, Y. and K.-N. N. Liou, "Solar radiative transfer in cirrus clouds. Part I: Single-scattering and optical properties of hexagonal ice crystals," *J. Atmos. Sci.*, Vol. 46, No. 1, 3–19, Jan. 1989.
43. Macke, A., "Scattering of light by polyhedral ice crystals," *Appl. Opt.*, Vol. 32, No. 15, 2780–2788, May 1993.
44. Macke, A., J. Mueller, and E. Raschke, "Single scattering properties of atmospheric ice crystals," *J. Atmos. Sci.*, Vol. 53, No. 19, 2813–2825, Oct. 1996.
45. Lock, J. A., "Ray scattering by an arbitrarily oriented spheroid, I: Diffraction and specular reflection," *Appl. Opt.*, Vol. 35, No. 3, 500–514, Jan. 1996.
46. Lock, J. A., "Ray scattering by an arbitrarily oriented spheroid, II: Transmission and cross-polarization effects," *Appl. Opt.*, Vol. 35, No. 3, 515–531, Jan. 1996.
47. Yang, P. and K. N. Liou, "Geometric-optics—integral-equation method for light scattering by nonspherical ice crystals," *Appl. Opt.*, Vol. 35, No. 33, 6568–6584, Nov. 1996.
48. Lorenz, L., "Lysbevaegelsen i og uden for en af plane Lysbolger belyst Kugle," *Det Kongelige Danske Videnskabernes Selskabs Skrifter*, Vol. 6, No. 6, 1–62, 1890.
49. Mie, G., "Beiträge zur Optik trüber Medien, speziell kolloidaler Metallösungen," *Ann. Phys.*, Vol. 330, No. 3, 377–445, 1908.
50. Yang, P. and K. N. Liou, "Light scattering by hexagonal ice crystals: Solutions by a ray-by-ray integration algorithm," *J. Opt. Soc. Am. A*, Vol. 14, No. 9, 2278–2289, Sep. 1997.
51. Muinonen, K., "Scattering of light by crystals: A modified Kirchhoff approximation," *Appl. Opt.*, Vol. 28, No. 15, 3044–3050, Aug. 1989.
52. Jackson, J. D., *Classical Electrodynamics*, 2nd edition, Wiley, Inc., New York, 1975.
53. Bi, L., P. Yang, G. W. Kattawar, Y. Hu, and B. A. Baum, "Scattering and absorption of light by ice particles: Solution by a new physical-geometric optics hybrid method," *J. Quant. Spectrosc. Radiat. Transf.*, Vol. 112, No. 9, 1492–1508, Jun. 2011.
54. Sun, B., P. Yang, G. W. Kattawar, and X. Zhang, "Physical-geometric optics method for large size faceted particles," *Opt. Express*, Vol. 25, No. 20, 24044–24060, Oct. 2017.

55. Van Diedenhoven, B., et al., "Remote sensing of ice crystal asymmetry parameter using multi-directional polarization measurements — Part 1: Methodology and evaluation with simulated measurements," *Atmos. Meas. Tech.*, Vol. 5, No. 10, 2361–2374, Oct. 2012.
56. Van Diedenhoven, B., B. Cairns, A. M. Fridlind, A. S. Ackerman, and T. J. Garrett, "Remote sensing of ice crystal asymmetry parameter using multi-directional polarization measurements — Part 2: Application to the Research Scanning Polarimeter," *Atmos. Chem. Phys.*, Vol. 13, No. 6, 3125–3203, Mar. 2013.
57. Van Diedenhoven, B., A. S. Ackerman, B. Cairns, and A. M. Fridlind, "A flexible parameterization for shortwave optical properties of ice crystals," *J. Atmos. Sci.*, Vol. 71, No. 5, 1763–1782, May 2014.
58. Bohren, C. F. and D. R. Huffman, *Absorption and Scattering of Light by Small Particles*, Wiley, New York, 1983.
59. Mishchenko, M., L. Travis, and A. Lacis, *Scattering, Absorption, and Emission of Light by Small Particles*, Cambridge University Press, 2002.
60. Quirantes, A., "A T-matrix method and computer code for randomly oriented, axially symmetric coated scatterers," *J. Quant. Spectrosc. Radiat. Transf.*, Vol. 92, No. 3, 373–381, May 2005.
61. Havemann, S. and A. J. Baran, "Extension of T-matrix to scattering of electromagnetic plane waves by non-axisymmetric dielectric particles: Application to hexagonal ice cylinders," *J. Quant. Spectrosc. Radiat. Transf.*, Vol. 70, No. 2, 139–158, Jul. 2001.
62. Kahnert, M., "The T-matrix code Tsym for homogeneous dielectric particles with finite symmetries," *J. Quant. Spectrosc. Radiat. Transf.*, Vol. 123, 62–78, Jul. 2013.
63. Kahnert, M., "T-matrix computations for particles with high-order finite symmetries," *J. Quant. Spectrosc. Radiat. Transf.*, Vol. 123, 79–91, Jul. 2013.
64. Tai, C. T., *Dyadic Green Functions in Electromagnetic Theory*, 2nd edition, IEEE Press, New York, 1994.
65. Hovenier, J. W., C. van der Mee, and H. Domke, *Transfer of Polarized Light in Planetary Atmospheres*, Springer, Dordrecht, 2004.
66. Mishchenko, M. I. and M. A. Yurkin, "On the concept of random orientation in far-field electromagnetic scattering by nonspherical particles," *Opt. Lett.*, Vol. 42, No. 3, 494–497, Feb. 2017.
67. Hu, C. R., G. W. Kattawar, M. E. Parkin, and P. Herb, "Symmetry theorems on the forward and backward scattering Mueller matrices for light scattering from a nonspherical dielectric scatterer," *Appl. Opt.*, Vol. 26, No. 19, 4159–4173, Oct. 1987.
68. Tsang, L., J. A. Kong, and R. T. Shin, *Theory of Microwave Remote Sensing*, Wiley-Interscience, New York, 1985.
69. Ren, K. F., F. Onofri, C. Rozé, and T. Girasole, "Vectorial complex ray model and application to two-dimensional scattering of plane wave by a spheroidal particle," *Opt. Lett.*, Vol. 36, No. 3, 370–372, Feb. 2011.
70. Sun, B., G. W. Kattawar, P. Yang, and K. F. Ren, "Rigorous 3-D vectorial complex ray model applied to light scattering by an arbitrary spheroid," *J. Quant. Spectrosc. Radiat. Transf.*, Vol. 179, 1–10, Aug. 2016.
71. Morse, P. and H. Feshbach, *Methods of Theoretical Physics*, McGraw-Hill, New York, 1953.
72. Foley, J. D., A. van Dam, S. K. Feiner, and J. F. Hughes, *Computer Graphics: Principles and Practice*, Addison-Wesley, Boston, MA, 1997.
73. Cauchy, A., "Memoire sur la rectification des courbes et la quadrature des surfaces courbes," *Mem. Acad. Sci. Paris*, 22, 3ff, 1950.
74. Vouk, V., "Projected area of convex bodies," *Nature*, Vol. 162, No. 4113, 330–331, Aug. 1948.
75. Xie, Y., P. Yang, G. W. Kattawar, B. A. Baum, and Y. Hu, "Simulation of the optical properties of plate aggregates for application to the remote sensing of cirrus clouds," *Appl. Opt.*, Vol. 50, No. 8, 1065–1081, Mar. 2011.
76. Chang, P. C. Y., J. G. Walker, and K. I. Hopcraft, "Ray tracing in absorbing media," *J. Quant. Spectrosc. Radiat. Transf.*, Vol. 96, Nos. 3–4, 327–341, Dec. 2005.

77. Brillouin, L., "The scattering cross section of spheres for electromagnetic waves," *J. Appl. Phys.*, Vol. 20, No. 11, 1110–1125, Nov. 1949.
78. Sun, B., P. Yang, G. W. Kattawar, and M. I. Mishchenko, "On Babinet's principle and diffraction associated with an arbitrary particle," *Opt. Lett.*, Vol. 42, No. 23, 5026–5029, Dec. 2017.
79. Ishimoto, H., K. Masuda, Y. Mano, N. Orikasa, and A. Uchiyama, "Irregularly shaped ice aggregates in optical modeling of convectively generated ice clouds," *J. Quant. Spectrosc. Radiat. Transf.*, Vol. 113, No. 8, 632–643, May 2012.
80. Yang, P., et al., "Spectrally consistent scattering, absorption, and polarization properties of atmospheric ice crystals at wavelengths from 0.2 to 100 µm," *J. Atmos. Sci.*, Vol. 70, No. 1, 330–347, Jan. 2013.
81. Bi, L., P. Yang, G. W. Kattawar, and R. Kahn, "Modeling optical properties of mineral aerosol particles by using nonsymmetric hexahedra," *Appl. Opt.*, Vol. 49, No. 3, 334–342, Jan. 2010.
82. Yang, P. and K. N. Liou, "Single-scattering properties of complex ice crystals in terrestrial atmosphere," *Contr. Atmos. Phys.*, Vol. 71, No. 2, 223–248, 1998.
83. Volten, H., O. Muñoz, J. W. Hovenier, and L. B. F. M. Waters, "An update of the Amsterdam light scattering database," *J. Quant. Spectrosc. Radiat. Transf.*, Vol. 100, Nos. 1–3, 437–443, Jul. 2006.
84. Nakajima, T., M. Tanaka, M. Yamano, M. Shiobara, K. Arao, and Y. Nakanishi, "Aerosol optical characteristics in the yellow sand events observed in May 1982 in Nagasaki: Part 2, models," *J. Meteorol. Soc. Japan Ser. II*, Vol. 67, No. 2, 279–291, 1989.
85. Okada, K., A. Kobayashi, Y. Iwasaka, H. Naruse, T. Tanaka, and O. Nemoto, "Features of individual Asian dust-storm particles collected at Nagoya, Japan," *J. Meteorol. Soc. Japan*, Vol. 65, No. 3, 515–521, 1987.
86. Reid, E. A., "Characterization of African dust transported to Puerto Rico by individual particle and size segregated bulk analysis," *J. Geophys. Res.*, Vol. 108, No. D19, 8591, Oct. 2003.
87. Hill, S. C., A. C. Hill, and P. W. Barber, "Light scattering by size/shape distributions of soil particles and spheroids," *Appl. Opt.*, Vol. 23, No. 7, 1025–1031, Apr. 1984.
88. Mishchenko, M. I., A. A. Lacis, B. E. Carlson, and L. D. Travis, "Nonsphericity of dust like tropospheric aerosols: Implications for aerosol remote sensing and climate modeling," *Geophys. Res. Lett.*, Vol. 22, No. 9, 1077–1080, May 1995.
89. Mishchenko, M. I., L. D. Travis, R. A. Kahn, and R. A. West, "Modeling phase functions for dustlike tropospheric aerosols using a shape mixture of randomly oriented polydisperse spheroids," *J. Geophys. Res. Atmos.*, Vol. 102, No. D14, 16831–16847, Jul. 1997.
90. Dubovik, O., et al., "Application of spheroid models to account for aerosol particle nonsphericity in remote sensing of desert dust," *J. Geophys. Res. Atmos.*, Vol. 111, No. D11, D11208, Jun. 2006.
91. Deschamps, P. Y., et al., "The POLDER mission: Instrument characteristics and scientific objectives," *IEEE Trans. Geosci. Remote Sens.*, Vol. 32, No. 3, 598–615, May 1994.
92. Labonnote, L. C., G. Brogniez, J. C. Buriez, M. Doutriaux-Boucher, J. F. Gayet, and A. Macke, "Polarized light scattering by inhomogeneous hexagonal monocrystals: Validation with ADEOS-POLDER measurements," *J. Geophys. Res.*, Vol. 106, No. D11, 12139–12153, Jun. 2001.
93. Huang, X., P. Yang, G. Kattawar, and K. N. Liou, "Effect of mineral dust aerosol aspect ratio on polarized reflectance," *J. Quant. Spectrosc. Radiat. Transf.*, Vol. 151, 97–109, Jan. 2015.
94. Cox, C. and W. Munk, "Measurement of the roughness of the sea surface from photographs of the sun's glitter," *J. Opt. Soc. Am.*, Vol. 44, No. 11, 838–850, Nov. 1954.
95. Stegmann, P. G. and P. Yang, "A regional, size-dependent, and causal effective medium model for Asian and Saharan mineral dust refractive index spectra," *J. Aerosol Sci.*, Vol. 114, 327–341, Dec. 2017.
96. Jarvis, R. A., "On the identification of the convex hull of a finite set of points in the plane," *Inf. Process. Lett.*, Vol. 2, No. 1, 18–21, Mar. 1973.
97. ElGindy, H., H. Everett, and G. Toussaint, "Slicing an ear using prune-and-search," *Pattern Recognit. Lett.*, Vol. 14, No. 9, 719–722, Sep. 1993.